JOURNAL OF GEOPHYSICAL RESEARCH, VOL. 105, NO. D14, PAGES 17,853–17,873, JULY 27, 2000

Global three-dimensional simulation of aerosol optical thickness distribution of various origins

Toshihiko Takemura,[1] Hajime Okamoto,[2] Yoshihiro Maruyama,[1] Atusi Numaguti,[3] Akiko Higurashi,[4] and Teruyuki Nakajima[1]

Abstract. A global three-dimensional model that can treat transportation of various species of aerosols in the atmosphere is developed using a framework of an atmospheric general circulation model (AGCM). Main aerosols in the troposphere, i.e., soil dust, carbonaceous (organic and black carbon), sulfate, and sea-salt aerosols, are introduced into this model. Prior to the model calculations the meteorological parameters are calculated by the AGCM with the nudging technique using reanalysis data. To evaluate aerosol effects on the climate system and to compare simulated results with observations, the optical thickness and Ångström exponent are also calculated taking into account the size distribution and composition. The model results are validated by both measured surface aerosol concentrations and retrieved aerosol optical parameters from National Oceanic and Atmospheric Administration/Advanced Very High Resolution Radiometer. A general agreement is found between the simulated result and the observation globally and seasonally. One of the significant results is that the simulated relative contribution of anthropogenic carbonaceous aerosols to the total optical thickness is comparable to that of sulfate aerosols at midlatitudes of the Northern Hemisphere, which agrees with recent observations. This result leads to a conclusion that the radiative effect evaluation of aerosols on the climate system is necessary to be modified because optical properties of carbonaceous aerosols are different from those of sulfate aerosols. The other finding is that the seasonal shift off the west coast of North Africa observed by satellites, i.e., the latitude of the maximum optical thickness moves seasonally, is also reproduced in consideration of a mixed state of soil dust and carbonaceous aerosols.

1. Introduction

It is important to estimate the climate forcing by anthropogenic and natural aerosols for predicting the future climate change. The global distributions of long-lived greenhouse gases are quantitatively well known and they cause positive radiative forcing. The total aerosol forcing is, on the other hand, evaluated as negative, i.e., cooling effect [e.g., *IPCC*, 1996]. The aerosol distribution is, however, highly uncertain because of their short lifetime, various chemical components, and size distributions. There may be two effects that aerosols affect the climate system. One is a direct effect that aerosols scatter and absorb the solar and infrared radiation [e.g., *Charlson et al.*, 1992], and the other is an indirect effect that aerosols alter the cloud properties acting as cloud condensation nuclei (CCN), and leading to a cloud albedo change [e.g., *Twomey*, 1974]. According to *IPCC* [1996], the total direct aerosol forcing was estimated to be -0.5 W m^{-2} with a large uncertainty of a factor of 2. Moreover, the total indirect forcing was estimated to be in a wide range from 0 to -1.5 W m^{-2} because the cloud-aerosol interaction process itself has been scarcely understood.

To minimize these uncertainties, an adequate aerosol transport model is necessary to be developed for simulating the aerosol distribution of various species. There have been many studies of three-dimensional models for sulfate aerosols, which have been considered to be dominant anthropogenic aerosols [*Langner and Rodhe*, 1991; *Pham et al.*, 1995; *Chin et al.*, 1996; *Feichter et al.*, 1996]. Recent measurements have shown, however, that carbonaceous aerosols are in many cases more predominant even in industrial regions [*Hegg et al.*, 1997; *Novakov et al.*, 1997]. The large optical thickness of carbonaceous aerosols originating from biomass burning also started to be recognized as noticeable from space [*Herman et al.*, 1997; *Nakajima and Higurashi*, 1998]. In spite of such a renewed attention to the climate effects of carbonaceous aerosols, there have been few global transport models for them [*Liousse et al.*, 1996]. Soil dust aerosols are also another important aerosol species, which contribute to a large-particle mass loading in the atmosphere. Several transport models were developed for the soil dust [*Joussaume*, 1990; *Tegen and Fung*, 1995; *Dentener et al.*, 1996].

Past studies concerning aerosol transport modeling were validated mostly by ground-based measurements of aerosol concentrations at some locations. However, ground-based measurements for aerosol concentrations are limited and include local variance, and therefore it is difficult to obtain a proper validation on global scale. In recent years, on the other hand, large amounts of satellite products for aerosols have become available as the result of the new progress in remote sensing technologies. For example, *Higurashi and Nakajima* [1999] analyzed the global distribution of the aerosol optical thickness and the Ångström exponent that is an index of the particle size (a large-particle polydispersion has a small Ångström exponent) using National Oceanic and Atmos-

[1]Center for Climate System Research, University of Tokyo, Tokyo.
[2]Kashima Space Research Center, Communications Research Laboratory, Ibaraki, Japan.
[3]Graduate School of Environmental Earth Science, Hokkaido University, Hokkaido, Japan.
[4]National Institute for Environmental Studies, Tsukuba, Japan.

Paper number 2000JD900265.
0148-0227/00/2000JD900265$09.00

pheric Administration (NOAA)/Advanced Very High Resolution Radiometer (AVHRR) data. It is very important therefore to find a method for comparing global optical remote sensing data with model values. In this regard, the situation of most of the past aerosol model studies has not been satisfactory since they simulated distributions of only one kind of aerosols, whereas the remotely sensed data are of a mixed state of several kinds of aerosols. *Tegen et al.* [1997] estimated the combined optical thickness of four species of aerosols by collecting results of different transport models for each aerosol type (soil dust [*Tegen and Fung*, 1995], carbonaceous [*Liousse et al.*, 1996], sulfate [*Chin et al.*, 1996], and sea salt [*Tegen et al.*, 1997]) and fixing the typical specific extinction cross section of each aerosol. Such a treatment is not necessarily appropriate for estimating the relative contribution of each aerosol type to the optical thickness, because the change in optical properties depending on the relative humidity was not considered, and because the transporting and scavenging processes are not the same among the models with different wind and cloud/rain fields.

In this study we develop a global three-dimensional model that can treat various aerosol species to overcome several drawbacks in the past aerosol modeling studies as mentioned above. Much attention is paid to the reproduction of not only the surface concentration but also the vertical column loading, comparing the result with the optical thickness from AVHRR retrievals in order to estimate the aerosol effects on the climate system. The common model structure to all aerosol species will be described in section 2. Characteristics for each aerosol type (soil dust, carbonaceous, sulfate, and sea salt), including emission sources and chemical reactions will be summarized in section 3. Mixing of all four aerosol species will be discussed in section 4 in terms of the total aerosol optical thickness and the Ångström exponent, and we will compare the model results with AVHRR retrievals [*Higurashi and Nakajima*, 1999; *Higurashi et al.*, 1999]. This comparison, as one of unique points of this study, becomes possible because of the global distribution of the optical properties obtained from AVHRR retrievals and that of the modeled four-component aerosol mixture. The simulated results also will be compared with ground-based optical observations of Aerosol Robotic Network (AERONET). Moreover, we will discuss a mechanism of the seasonal shift of the maximum optical thickness off the west coast of North Africa as observed by satellites. Our conclusions will be presented in section 5.

2. Model Description

The present three-dimensional aerosol model uses a framework of Center for Climate System Research (CCSR), University of Tokyo/National Institute for Environmental Studies (NIES), Japan, atmospheric general circulation model (AGCM). The basic features of CCSR/NIES AGCM are presented by *Numaguti* [1993], and newly implemented physical processes are discussed by *Numaguti et al.* [1995]. This AGCM adopts a radiation scheme based on the *k*-distribution and the two-stream discrete ordinate method [*Nakajima and Tanaka*, 1986]. In our simulation the horizontal resolution is set at about 5.6° longitude by 5.6° latitude (T21, i.e., triangular truncation with wavenumber 21), the vertical resolution at 11 layers (sigma levels at 0.995, 0.980, 0.950, 0.900, 0.815, 0.679, 0.513, 0.348, 0.203, 0.092, and 0.021), and time step at 40 min. This aerosol transport model mainly includes processes of emission, advection, diffusion, and deposition. The equation of aerosol mass conservation is as follows:

$$\frac{\partial}{\partial t}(\rho_{\mathrm{air}} q_a) + div(\rho_{\mathrm{air}} q_a \mathbf{v}) + \frac{\partial}{\partial z}(\rho_{\mathrm{air}} q_a w) = \frac{\partial}{\partial z}(F_E + F_D + F_S), \quad (1)$$

where ρ_{air} is the air density, q_a is the aerosol mixing ratio, and $\mathbf{v}$ and w are horizontal and vertical wind, respectively; F_E, F_D, and F_S are the emission, diffusion, and deposition fluxes of aerosols, respectively. The advection scheme for water vapor in the AGCM is applied to the aerosol advection. The right-hand side of equation (1) is newly modeled in this study as described in Appendix A. To compare simulated results with optical observations such as AVHRR retrievals and Sky/Sun photometer measurements, the optical thickness is also calculated at each time step using the calculated relative humidity. The detailed explanation for the calculation of the optical thickness is described in Appendix B.

This model uses National Centers for Environmental Prediction (NCEP)/National Center for Atmospheric Research (NCAR) reanalysis data of wind velocities, temperature, and specific humidity as a constraint. Every 2-hour data of meteorological parameters, such as diffusion coefficient, precipitation flux, and cloud water, which are necessary as input data for driving the transport model, are made by means of running the AGCM as nudged by NCEP/NCAR reanalysis data in 1990, because the results of this model are mainly compared with the satellite data of 1990 obtained from AVHRR retrievals.

The wind velocity at 10-m height is needed for evaluating emissions of soil dust and sea-salt aerosols. It is calculated from the wind velocity at the lowest layer of the AGCM (corresponding to about 50-m height) on the basis of the Monin-Obukhov similarity theory. In the unstable or stable condition the function depending on the Richardson number is also introduced [*Louis*, 1979]. Moreover, we consider small-scale dry convection with a large upward sensible heat flux in the evaluation of surface wind, which is pronounced in the case of strong wind.

3. Characteristics for Each Aerosol Type

3.1. Soil Dust Aerosols

It has been expected that soil dust aerosols have a large impact on the climate system based on satellite and ground-based observations [*Li et al.*, 1996; *Herman et al.*, 1997; *Moulin et al.*, 1997]. Soil dust particles scatter the solar radiation back to space and absorb the ultraviolet radiation. In this model, the particle size is divided into 10 radii from 0.1 to 10 μm for transport processes and the calculation of the optical thickness of soil dust aerosols. The effective radius and the normalized emission strength of each size are according to *d'Almeida and Schütz* [1983] (Table 1). The

Table 1. Effective Radius and Normalized Emission Strength for Soil Dust Aerosols in the Model

Radius Range, μm	Effective Radius, μm	Normalized Emission Strength
0.10 - 0.16	0.13	0.017
0.16 - 0.25	0.20	0.040
0.25 - 0.40	0.33	0.11
0.40 - 0.63	0.52	0.27
0.63 - 1.00	0.82	0.67
1.00 - 1.58	1.27	1.0
1.58 - 2.51	2.02	1.0
2.51 - 3.98	3.20	1.0
3.98 - 6.31	5.06	1.0
6.31 - 10.0	8.02	1.0

particle density of soil dust aerosols is assumed to be 2.5 g cm^{-3} [*Volz*, 1973].

Emission locations are limited to the desert, grassland, xeromorphic shrubland, and cultivated field defined by *Matthews* [1983]. The emission mass flux of soil dust F_{ed} in kg m^{-2} s^{-1} is given according to the empirical relation as follows [*Gillette*, 1978]:

$$F_{ed} = \begin{cases} C(|\mathbf{v}_{10}| - u_t)|\mathbf{v}_{10}|^2 & \text{for } |\mathbf{v}_{10}| \geq u_t, \\ 0 & \text{for } |\mathbf{v}_{10}| < u_t, \end{cases} \quad (2)$$

where $|\mathbf{v}_{10}|$ is the wind velocity at 10-m height in m s^{-1}, u_t is a threshold velocity set to be 6.5 m s^{-1} according to *Kalma et al.* [1988], and C is an emission coefficient depending on the soil moisture in kg s^2 m^{-5}. C is decided by fitting to the AVHRR optical thickness over ocean near dust regions such as the west coast of Sahara and the Arabian Sea:

$$C = \begin{cases} 1.5\times10^{-9} \times \dfrac{0.003 - W_g}{0.003} & \text{for } 0 \leq W_g \leq 0.003 \text{ (m m}^{-1}\text{)}, \\ 0 & \text{for } W_g > 0.003 \text{ (m m}^{-1}\text{)}, \end{cases} \quad (3)$$

where W_g is the soil moisture in m m^{-1}.

3.2. Carbonaceous Aerosols

Carbonaceous aerosols are roughly divided into two components, i.e., organic carbon (OC) and black carbon (BC). OC mainly scatters the solar radiation without significant absorption and grows absorbing ambient water vapor. On the other hand, BC strongly absorbs the solar radiation and is hydrophobic. In this model, the internal mixture of both carbons is assumed for transport processes and the optical thickness calculation. The particle radius depending on the relative humidity is determined from *Hobbs et al.* [1997] (Table 2), and the particle densities are assumed to be 1.5 g cm^{-3} and 1.25 g cm^{-3} for OC and BC, respectively [*Horvath*, 1993].

Sources for carbonaceous aerosols are classified into six categories: forest fires in tropical rain forests, those in other forests, fossil fuel consumption, fuel wood consumption, combustion of agricultural wastes, and gas to particle conversion of terpene emitted from plants. Carbonaceous aerosols emitted from forest fires are one of the most important contributions to the atmospheric turbidity. The Global Emissions Inventory Activity (GEIA) database of monthly BC emission from biomass burning [*Cooke and Wilson*, 1996] is used with a revision using a new data set for change in forest cover [*FAO*, 1997]. Furthermore, forest fire sources are divided into two species, i.e., tropical rain forests and other forests, because of a more incomplete burning condition over tropical regions, and hence a different ratio of OC to BC (OC/BC). For this classification, the vegetation data obtained from NOAA/AVHRR data are used [*DeFries and Townshend*, 1994]. The OC/BC ratio is assumed to be 8.28 and 6.92 for tropical and other forests, respectively, according to *Liousse et al.* [1996]. The GEIA database is also used for annual BC emission from fossil fuel [*Cooke and Wilson*, 1996]. The burning condition of fossil fuel is more complete than that of forest fires, and hence a small ratio of OC/BC is assumed to be 3.33 in this model [*Liousse et al.*, 1996]. Monthly BC emission data for fuel wood consumption and combustion of agricultural waste are obtained using *FAO* [1995a] and *FAO* [1995b] statistics in each country, respectively, and GEIA database for population and grid locations of each country according to *Liousse et al.* [1996]. The OC/BC ratio is assumed to be 5.64 and 6.92 for fuel wood consumption and combustion of agricultural waste, respectively [*Liousse et al.*, 1996]. The GEIA database for monthly terpene emissions is also used [*Guenther et al.*, 1995] assuming the conversion rate to OC particles to be 0.04 according to *Pandis et al.* [1991].

Table 2. Mode Radius of Carbonaceous Aerosol Particle Depending on the Relative Humidity in the Model

Relative Humidity, %	Mode Radius, μm
0 – 25	0.180
25 – 60	0.189
60 – 75	0.214
75 – 85	0.236
85 - 92.5	0.277
92.5 - 96.5	0.306
96.5 - 98.5	0.328
98.5 – 100	0.337

Table 3. Mode Radius of Sulfate Aerosol Particle Depending on the Relative Humidity in the Model

Relative Humidity, %	Mode Radius, μm
0 – 25	0.139
25 – 60	0.197
60 – 75	0.218
75 – 85	0.236
85 - 92.5	0.270
92.5 - 96.5	0.316
96.5 - 98.5	0.390
98.5 – 100	0.462

3.3. Sulfate Aerosols

Sulfate aerosols scatter the solar radiation without significant absorption, and it is hydrophilic. The growth rate of particle radius depending on the relative humidity is based on *Hänel* [1976] (Table 3), and the particle density is set as 1.769 g cm^{-3} [*Weast*, 1976] in this model.

Sulfate aerosols are formed mainly by chemical reactions of SO_2 and dimethylsulfide (DMS). DMS is emitted mainly from the oceanic phytoplankton and reacts with OH radical, so it is converted into SO_2 and sulfate through intermediates. SO_2, which is emitted from fossil fuel consumption and volcanic activities, is mainly oxidized by OH in the gas phase and H_2O_2 and O_3 in liquid phase, so it is converted into sulfate. There are some past studies about global sulfate distribution, but *Langner and Rodhe* [1991] and *Pham et al.* [1995] simplified the liquid phase reaction of SO_2, which is a main reaction forming sulfate aerosols. In this model, however, chemical reactions related to sulfate aerosols and SO_2 dissolution into water are treated explicitly. The SO_2 dissolution process is also applied to the in-cloud scavenging of SO_2. Table 4 summarizes chemical reactions and reaction rate constants, and solubility and equilibrium constants are also shown in Table 5 and Table 6, respectively. The zonally and seasonally averaged OH distribution is given by the result of the other chemical model [*Spivakovsky et al.*, 1990]. The zonally and 6-month averaged O_3 distribution and the globally and annual mean vertical H_2O_2 distribution in this model are also given by the definition in LOWTRAN 7 [*Kneizys et al.*, 1990]. The DMS emission flux F_{DMS} in kg m^{-2} s^{-1} over the ocean is proportional to the

Table 4. Chemical Reactions and Rate Constants in the Model

Reaction	Reaction Rate[a]	Reference[b]
DMS → SO_2, sulfate		
$DMS + OH \rightarrow SO_2 + \cdots$	$k_1 = 9.6\times10^{-12}\exp(-234/T)$	(a), (b)
$\begin{cases} DMS + OH \rightarrow 0.6SO_2 + 0.4DMSO + \cdots \\ DMSO + OH \rightarrow 0.6SO_2 + 0.4SO_4^{2-} + \cdots \end{cases}$	$k_2 = 3.04\times10^{-12}\exp(350/T)\times\frac{\alpha}{1+\alpha}$ $\alpha = 1.106\times10^{-31}\exp(7460/T)\times[M]$	(a), (b)
SO_2 → sulfate		
$SO_2 + OH \rightarrow SO_4^{2-} + \cdots$	$k_3 = \frac{\alpha_o[M]}{1+\frac{\alpha_o[M]}{\alpha_\infty}}\times0.6^{\frac{1}{1+[\log_{10}(\alpha_o[M]/\alpha_\infty)]^2}}$ $\alpha_o = 3\times10^{-31}\times(300/T)^{3.3}$ $\alpha_\infty = 1.5\times10^{-12}$	(c)
$S(IV) + O_3(aq) \rightarrow SO_4^{2-} + O_2$	$k_4 = \frac{k_a + \frac{k_bK_1}{[H^+]} + \frac{k_cK_1K_2}{[H^+]^2}}{1+\frac{K_1}{[H^+]}\left(1+\frac{K_2}{[H^+]}\right)}$ $k_a = 2.0\times10^{4}$ $k_b = 3.2\times10^{5}$ $k_c = 1.0\times10^{9}$	(d)
$S(IV) + H_2O_2(aq) \rightarrow SO_4^{2-} + H_2O$	$k_5 = \frac{k_d[H^+]}{\left(k_e+[H^+]\right)\left(1+\frac{[H^+]}{K_1}+\frac{K_2}{[H^+]}\right)}$ $k_d = 5.6\times10^{6}$ $k_e = 0.1$	(d)

[a]Values k_1, k_2, and k_3 are in cm^3 molecule^{-1} s^{-1}, k_4 and k_5 are in l mole^{-1} s^{-1}, T is the temperature in Kelvin, [M] is the air number concentration in cm^{-3}, $[H^+]$ is the hydrogen ion concentration in mole l^{-1}, K_1 and K_2 are equilibrium constants (see Table 6), k_a, k_b, k_c, and k_d are in l mole^{-1} s^{-1}, and k_e is in mole l^{-1}.

[b]References are (a) *Hynes et al.* [1986], (b) *Chatfield and Crutzen* [1990], (c) *DeMore et al.* [1997], and (d) *Warneck* [1988].

downward surface solar flux F_{rad} in W m^{-2} in this model [*Bates et al.*, 1987],

$$F_{DMS} = 1.08\times10^{-14}\times F_{rad} + 3.56\times10^{-13}. \quad (4)$$

The monthly data of sea-ice mask [*da Silva*, 1994] is used for DMS not to be emitted from areas covered by sea ice. The GEIA database are used for SO_2 originating from fossil fuel consumption and metal production [*Benkovitz et al.*, 1996] and from continuously erupting volcanoes [*Andres and Kasgnoc*, 1998].

3.4. Sea-Salt Aerosols

The importance of sea-salt aerosols for the climate system is to be seen in connection with its potential source areas, which cover about two thirds of the Earth's surface. Sea-salt particle has a larger radius than that of carbonaceous and sulfate aerosols. The particle size of sea-salt aerosols is divided into 10 effective radii from 0.1 μm to 10 μm assuming the a lognormal size distribution for transport processes and for the calculation of the optical thickness with a standard deviation assumed as 2.0 [*d'Almeida et al.*, 1991] (Table 7). The particle density is set as 2.25 g cm^{-3} in this model [*Hänel*, 1976]. Sea-salt particles have a cubic shape, so the Mie theory cannot be strictly applied. We calculated the nonspherical scattering effect by a discrete dipole approximation method [*Okamoto et al.*, 1995; *Murayama et al.*, 1999]. The difference of the extinction efficiency factor between Mie particles and cubic particles is found to be less than 5% for the particle radius less than 0.4 μm; the difference is slightly larger for large radii but not more than 20%. Therefore we decided to use the Mie theory for calculating the optical thickness in this model.

Sea-salt aerosols are produced by breaking bubbles of seawater at ocean surface, and therefore the emission flux depends significantly on the surface wind velocity. This model uses the empirical formula of *Erickson et al.* [1986] for the surface concentration C_{sa} in μg m^{-3},

$$C_{sa} = \begin{cases} \exp(0.16|v_{10}|+1.45) & \text{for } |v_{10}|\le 15 \text{ (m s}^{-1}\text{)}, \\ \exp(0.13|v_{10}|+1.89) & \text{for } |v_{10}|> 15 \text{ (m s}^{-1}\text{)}. \end{cases} \quad (5)$$

The surface concentration C_{sa} is calculated at each time step, and the difference of the concentration between before and after the time step is regarded as the emission flux. The mass mean radius r_{mm} in micron is also estimated as follows [*Erickson and Duce*, 1988]:

Table 5. Solubility Constants in the Model

Reaction	Solubility Constant, mole l^{-1} atm^{-1}
$(SO_2)_g \rightleftarrows (SO_2)_{aq}$	$K_{SO_2} = 1.23\exp\left[3120\left(\frac{1}{T}-\frac{1}{298}\right)\right]$
$(O_3)_g \rightleftarrows (O_3)_{aq}$	$K_{O_3} = 1.15\times10^{-2}\exp\left[2560\left(\frac{1}{T}-\frac{1}{298}\right)\right]$
$(H_2O_2)_g \rightleftarrows (H_2O_2)_{aq}$	$K_{H_2O_2} = 9.7\times10^{-4}\exp\left[6600\left(\frac{1}{T}-\frac{1}{298}\right)\right]$

After *Chameides* [1984].

Table 6. Equilibrium Constants in the Model

Reaction	Equilibrium Constant, mole l^{-1}
$(SO_2)_{aq} + H_2O \rightleftarrows H^+ + HSO_3^-$	$K_1 = 1.7\times10^{-2}\exp\left[2090\left(\frac{1}{T}-\frac{1}{298}\right)\right]$
$HSO_3^- \rightleftarrows H^+ + SO_3^{2-}$	$K_2 = 6\times10^{-8}\exp\left[1120\left(\frac{1}{T}-\frac{1}{298}\right)\right]$

After *Chameides* [1984].

Table 7. Effective Radius and Corresponding Mass Mean Radius of Sea-Salt Aerosols in the Model

Radius Range, μm	Effective Radius, μm	Mass Mean Radius, μm
0.100 - 0.159	0.126	0.682
0.159 - 0.251	0.200	1.07
0.251 - 0.398	0.316	1.68
0.398 - 0.631	0.501	2.56
0.631 - 1.00	0.794	3.67
1.00 - 1.59	1.26	4.84
1.59- 2.51	2.00	5.88
2.51 - 3.98	3.16	6.70
3.98 - 6.31	5.01	7.31
6.31 - 10.0	7.77	7.77

$$r_{mm} = 0.422 \mid v_{10} \mid + 2.12. \quad (6)$$

This mass mean radius is used to determine the mode radius of the lognormal size distribution by selecting the nearest value in Table 7. The sea-salt emission is inhibited over sea-ice regions in the same manner as in the case of the DMS emission.

4. Results and Discussion

4.1. Global Distribution for Each Aerosol Type

The annual mean global distributions of the simulated surface concentration and the optical thickness at a wavelength of 0.55 μm for soil dust, carbonaceous, sulfate, and sea-salt aerosols are shown in Figures 1 and 2, respectively. Saharan dust particles are transported by the trade wind over the North Atlantic throughout the year. A large amount of soil dust is also seen around the Arabian Sea in the Northern Hemisphere summer, which can be explained by the strong monsoon wind in this season. Carbonaceous aerosols originating from biomass burning are prominent in the center and south of Africa and South America. Biomass burning events occur during the dry season of each region and are observed as hot spots from space [*Cahoon et al.*, 1992; *Andreae*, 1993]. Carbonaceous aerosols are also emitted from industrial regions with consumption of fossil and domestic fuels almost regularly through the year at midlatitudes of the Northern Hemisphere. A high concentration of sulfate aerosols originating from anthropogenic sources is seen in East Asia, Europe, and North America through the year. In case of sea-salt aerosols the maximum concentration is seen over the Antarctic Sea at 50°-60°S through the year as well as over the North Atlantic and the North Pacific. On the other hand, the optical thickness of sea-salt aerosols is large in tropical regions and midlatitudes because of the strong vertical diffusion. Their optical thickness is, however, much smaller than that of other aerosols in spite of large surface concentrations because the extinction efficiency per mass is small due to large-particle radii.

Simulated surface concentrations are compared with observed ones for carbonaceous (Tables 8 and 9), DMS (Table 10), SO_2 (Table 11), and sulfate aerosols (Table 12) at some locations. Simulated concentrations of carbonaceous aerosols are reproduced well compared with observations. *Liousse et al.* [1996] simulated not only BC but also OC global distributions for the first time, but their results were largely underestimated OC and BC concentrations in comparison with observations in midlatitudes of the Northern Hemisphere as pointed out by the authors themselves. This underestimation is, however, not seen in our simulation (Table 9). Simulated DMS concentrations are also in agreement with observed ones within a difference of about 40%. On the other hand, simulated SO_2 and sulfate concentrations are somewhat underestimated and overestimated, respectively, in industrial regions. This might be because changes in SO_2, H_2O_2, and O_3 concentrations within each time step are neglected in this model, though the liquid phase reaction proceeds to completion in less than 1 hour [*Chin et al.*, 1996]. It is, however, general agreement between simulated and observed concentrations of SO_2 and sulfate aerosols other than in industrial regions. Figure 3 shows that the monthly mean simulated surface concentrations for sea-salt aerosols reasonably agree with the observed ones seasonally and quantitatively in Barbados and Midway. Simulated surface concentrations of sea-salt aerosols in other regions are expected not to be largely different from observations because the distribution of sea-salt aerosols is not as inhomogeneous as that of soil dust, carbonaceous, and sulfate aerosols.

Figure 4 shows simulated and observed vertical profiles of soil dust aerosols in Barbados, carbonaceous aerosols over a biomass burning region, and sulfate aerosols over an industrial region. The observed feature of the large soil dust concentration between 1 km and 3 km altitude, so-called "dust layer," is reproduced to some extent, though the magnitude of the simulated concentration is underestimated. *Anderson et al.* [1996] analyzed the data obtained from aircraft measurements over biomass burning, finding the aerosol number concentration decreased almost monotonously with altitudes above 1.5 km over the source region, while they have the peak between 2 and 6 km over the outflow region. These tendencies are reproduced to some extent in this model though the altitude of the simulated maximum concentration is low over the outflow region. The decrease of the simulated sulfate concentration with altitudes is similar to that of the observed one.

Figure 5 summarizes the global amounts and the mass fluxes of aerosols simulated by the present model. The annual total emission fluxes of soil dust and sea-salt aerosols are 1 order larger than those of other aerosol species. The dry deposition flux of soil dust aerosols occupies 66% of the total flux, because of their large-particle radius and emission occurring mostly in arid or semiarid regions. The wet deposition fluxes of carbonaceous and sulfate aerosols, on the other hand, account for 82% and 88% of the total depositions, because of their hydrophilicity. The liquid phase oxidation of SO_2 is larger than the gas phase oxidation as commonly recognized [*Warneck*, 1988]. The lifetimes of DMS and SO_2 are consistent with other sulfur models [*Langner and Rodhe*, 1991; *Pham et al.*, 1995; *Chin et al.*, 1996; *Feichter et al.*, 1996], though that of sulfate aerosols is slightly shorter in this model (2.6 days).

4.2. Global Aerosol Optical Properties in a Mixed State

Figure 6 shows the simulated distributions of the combined monthly mean optical thickness of soil dust, carbonaceous, sulfate, and sea-salt aerosols in January, April, July, and October. Figure 7 also shows the simulated distributions of the monthly mean Ångström exponent defined as log slope of the spectral optical thickness at wavelengths of 0.55 μm and 1.0 μm. The most prominent contributors to the total aerosol loading are soil dust and carbonaceous aerosols. Soil dust aerosols are noticeable around Saharan and Arabian regions with a small Ångström exponent from about zero to 0.2, while carbonaceous aerosols originating from biomass burning are remarkable on the coast of the Gulf of Guinea in January and over the south of Africa and Amazon from July to October with a large Ångström exponent close to 1.0. These simulated geographical patterns of the optical

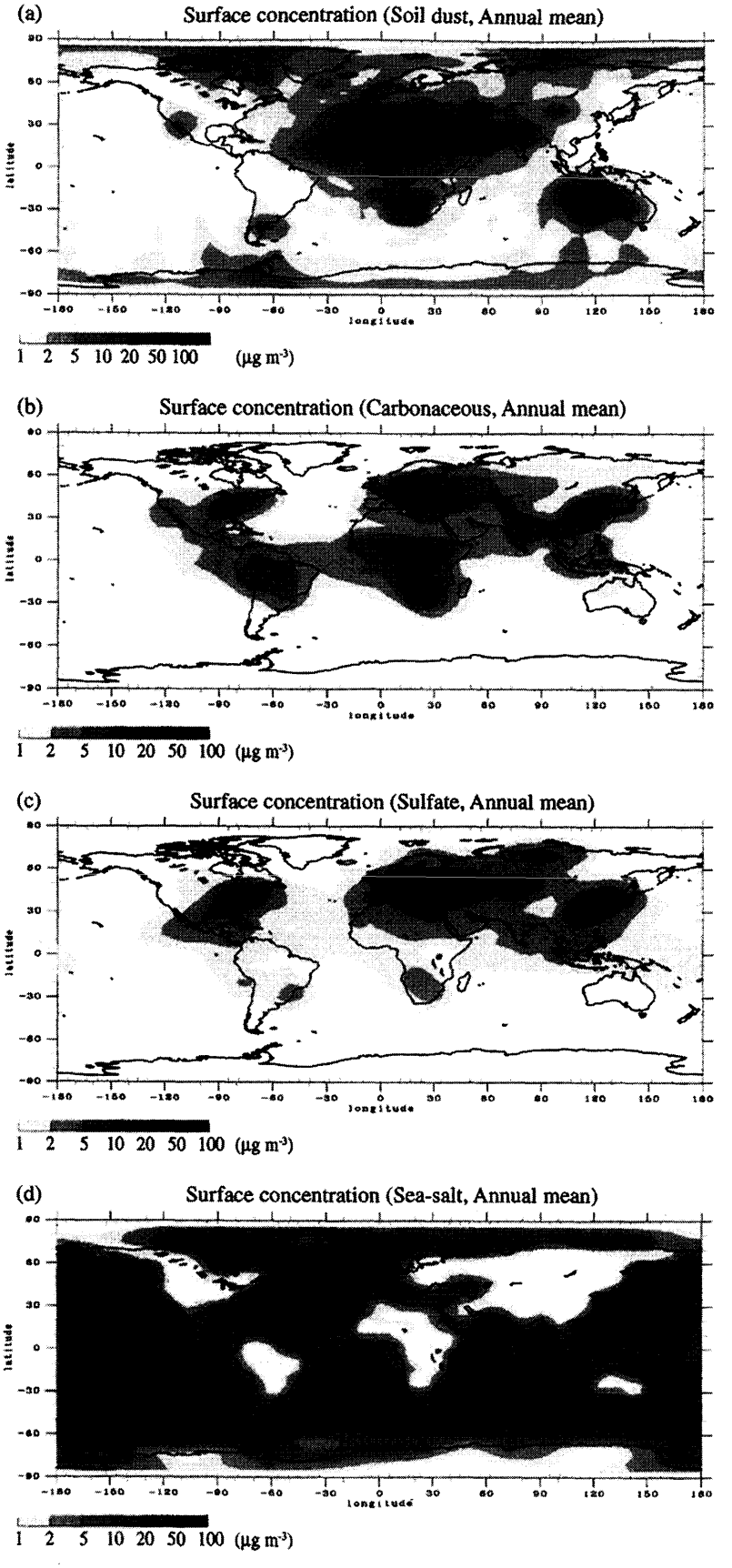

Figure 1. Annual mean distributions of the simulated surface concentrations for (a) soil dust, (b) carbonaceous, (c) sulfate, and (d) sea-salt aerosols in μg m^{-3}.

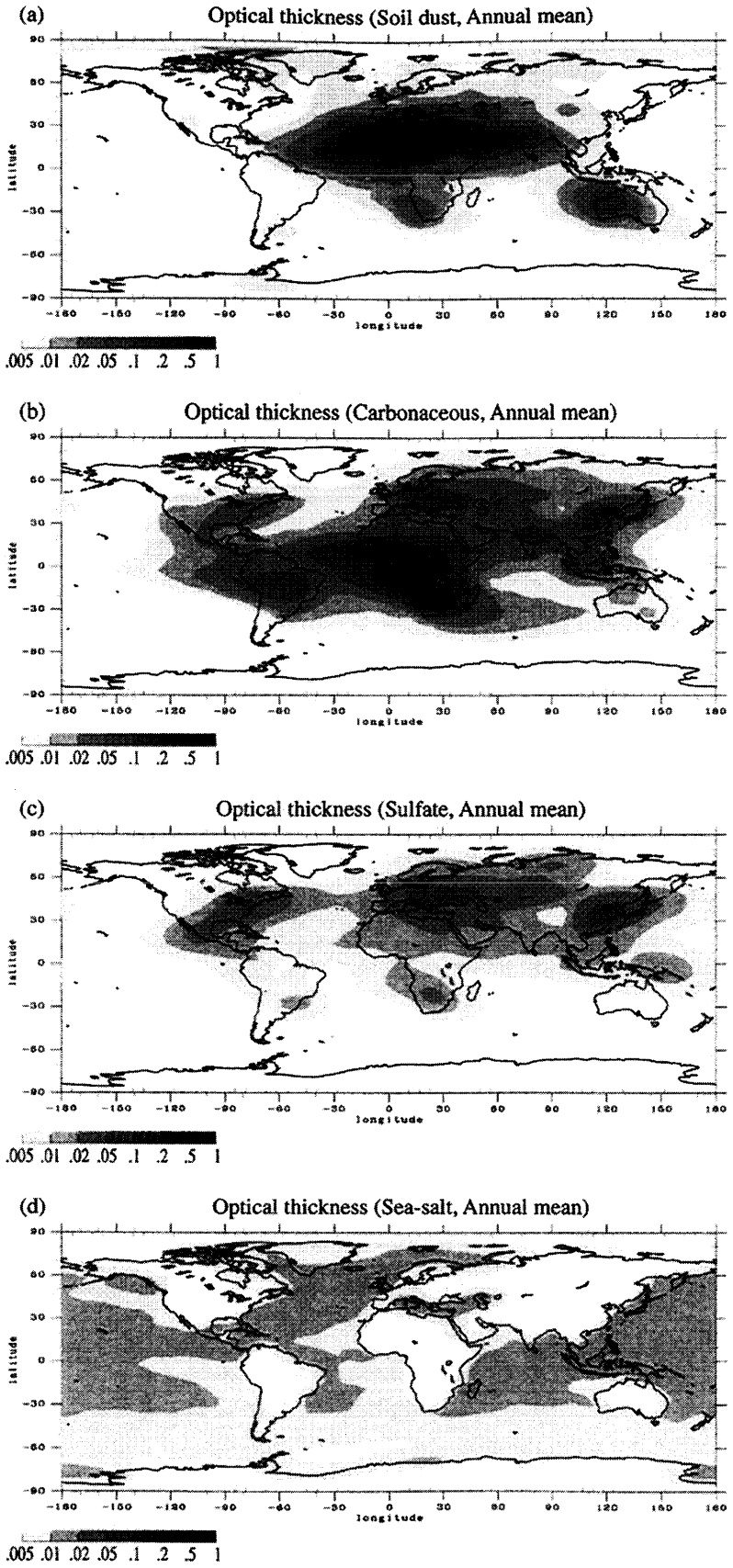

Figure 2. Annual mean distributions of the simulated optical thickness for (a) soil dust, (b) carbonaceous, (c) sulfate, and (d) sea-salt aerosols.

Table 8. Comparison between Simulated and Observed Concentrations of Carbonaceous Aerosols

Location	Time Period	Concentration, ng m^{-3}		Reference[a]
		Observation	Model	
OC + BC				
American Samoa (13.0°S, 172.0°W)	July – Aug., Jan. – Feb.	108	94	(a)
Amsterdam Island (38.0°S, 77.0°E)	Feb.	155	105	(a)
New Zealand (41.0°S, 174.0°E)	June – Aug.	130	118	(a)
OC				
Hawaii (21.4°N, 147.7°W)	Sept.	390	393	(b)
Puerto Rico (18.3°N, 65.8°W)	April	662	556	(c)
BC				
Beijing (40.0°N, 116.0°E)	July – Aug.	2163	2886	(d)
Mauna Loa (19.3°N, 155.4°W)	annual	5.82	2.13	(e)
South pole (87.0°S, 102.0°W)	annual	0.65	1.15	(e)

[a]Observed values: (a) *Cachier et al.* [1986], (b) *Hoffman and Duce* [1977], (c) *Novakov and Penner* [1993], (d) *Parungo et al.* [1994], and (e) *Bodhaine* [1995].

thickness and Ångström exponent are consistent with the patterns observed by satellites [*Nakajima and Higurashi*, 1998; *Higurashi et al.*, 1999]. Simulated optical thickness of biomass burning aerosols from the south of Africa extends to northwest and southeast directions, as supported by the AVHRR retrieval. In midlatitudes of the Northern Hemisphere, anthropogenic carbonaceous and sulfate aerosols prevail, showing the noticeably distinct seasonal variation with the maximum in summer. Investigation of the model results suggests three main reasons for this seasonal variability of the optical thickness. One is growth of aerosol particles absorbing ambient water vapor with higher relative humidity in summer over this region, causing an increase in extinction efficiency Q_{ext}. In the present model, Q_{ext} in the condition over the relative humidity of 90% is set about 5 times as large as in that of 25% for the mode radius. The second reason is large oxidation of SO_2 and DMS in summertime because of the high OH concentration. For instance, it is given as 19×10^5 molecules cm^{-3} at 36°N, 900 hPa in July, while 2.4×10^5 molecules cm^{-3} at the same location in January. The third is that aerosols and their precursors are difficult to fall out in summer because of large instability of the atmosphere. The lifetime of sulfate aerosols in summer is about 3 times as long as that in winter for the zonal mean of 36°N. The simulated Ångström exponent is also larger in summertime over midlatitudes of the Northern Hemisphere. These seasonal variabilities in optical thickness and Ångström exponent were detected by AVHRR retrievals over this region, as shown in section 4.3. Larger aerosol concentrations during spring to summer were also observed at a remote ocean site, Mauna Loa, Hawaii [*Lee et al.*, 1994]. These observations support adequacy of the aerosol growth model depending on the relative humidity shown in Tables 2 and 3 and the uplift scheme described in Appendix A.

Table 9. Comparison between Simulated and Observed Annual Mean Concentrations of Organic Carbon in the United States

Location	Concentration, ng m^{-3}		
	Observation	This Model	*Liousse et al.* [1996]
Appalachian	2950	3512	1010
Boundary water	2025	2211	430
Cascades	2850	1027	310
Colorado Plateau	1225	1301	420
Central Rockies	1425	1124	380
Central Coast	1975	2406	380
Great Basin	1125	873	330
Northern Great Plains	1525	1365	390
Northern Rockies	3175	976	300
Southern California	2650	1795	450
Sonora Desert	1475	1487	500
Sierra Nevada	2125	1795	410
Sierra-Humboldt	1575	1854	350
West Texas	1475	1624	570

Observed values: *Malm et al.* [1994]; simulated values: this study and *Liousse et al.* [1996].

4.3. Regional Features and Comparisons with Optical Observations

To examine the regional and seasonal features, regional averages of the simulated monthly mean optical thickness and Ångström exponent over ocean are compared with the AVHRR statistics [*Higurashi et al.*, 1999] for 4 months in 1990, i.e., in January, April, July, and October. Although there is some possibility of overestimation in the AVHRR optical thickness, especially in regions of small optical thickness (< 0.2), the AVHRR retrievals can be used for studying the simulated seasonal variations. Monthly mean values of AERONET data [*Holben et al.*, 1998] are also used for comparison over land. It is, however, necessary to be careful that AERONET data can include local variance to some extent because they are ground-based measurements and that AERONET observation years are different from the year of atmospheric field in 1990 used in the simulation.

4.3.1. Industrial regions. Figure 8 shows the simulated optical thickness for each aerosol type and a mixture of four aerosol species in midlatitudes of the Northern Hemisphere with the corresponding AVHRR retrievals or AERONET data. Over the United States the simulated optical thickness is not much different from the AERONET values seasonally and quantitatively (Figure 8a), while it is about 3 times smaller than the AVHRR optical thickness (Figure 8b). A similar difference between simulated and AVHRR optical thicknesses is seen over other industrial regions (Figures 8c, 8d, and 8e). The simulated contribution of soil dust aerosols transported from the Saharan region is large from spring to summer over the Black Sea and the Mediterranean. Around Japan, AVHRR retrievals detect the "Kosa" dust transported from the Gobi and Takla Makan Deserts in April, but the simulated column loading of soil dust aerosols is too small. This must be corrected by further improvements such as increasing the horizontal resolution in order to reproduce the realistic surface conditions and sources. At the same time, satellite values may be corrected by introducing a better optical model of Kosa aerosols. The simulated Ångström exponent is also smaller than observed values over the above five regions. This underestima-

Table 10. Comparison between Simulated and Observed DMS Concentrations

Location	Time Period	Concentration, pptv		Reference[a]
		Observation	Model	
Amsterdam Island (38°S, 78°E)	annual	112	153	(a)
Bahamas (20-25°N, 73-80°W)	June	154	225	(b)
	Nov.	122	103	(c)
Cape Grim (40.68°S, 144.68°E)	Jan.	167	202	(c)
Sargasso Sea (20-25°N, 73-80°W)	June	232	216	(c)
Equatorial Pacific (Ecuador - Hawaii)	July	115-196	105-194	(c)
Northeast Pacific (west of Seattle, United States)	April	75	96	(d)
Pacific (15-29°N, 170°W)	April - May	60	106-116	(e)
(11°S-14°N, 170°W)	April - May	269	148-204	(e)
Antarctic (56-63°S, 65-57°W)	Nov. – Dec.	147	129-185	(f)

[a]Observed values: (a) *Nguyen et al.* [1992], (b) *Saltzman and Cooper* [1988], (c) *Andreae et al.* [1985], (d) *Bandy et al.* [1992], (e) *Quinn et al.* [1990], and (f) *Staubes and Georgii* [1993].

tion may suggest that smaller mode radii are needed for more appropriate simulation. In spite of some differences between the simulation and the observations, simulated optical thickness indicates the maximum value from spring to summer as observed by AVHRR and AERONET.

In midlatitudes of the Northern Hemisphere where strong sources of anthropogenic pollutant exist, it has been common assumption that anthropogenic sulfate aerosols dominate in the optical thickness. The recent aircraft observations in the industrial region of the eastern United States, however, indicated that the concentration and optical thickness of carbonaceous aerosols are comparable with or larger than those of sulfate aerosols [*Hegg et al.*, 1997; *Novakov et al.*, 1997]. Therefore the relative contribution of carbonaceous aerosols to the optical thickness may be still larger over other industrial regions, such as Europe and East Asia, because fossil fuels of high carbon content are consumed in these regions. *Heintzenberg et al.* [1998] also suggested, based on the analysis of aerosol samplings, that organic compounds may be significant over the industrial region of Europe. In the present model, contributions of carbonaceous and sulfate aerosols are simulated to be comparable during all seasons (Figure 8), which is consistent with the above mentioned observations. *Tegen et al.* [1997], who estimated the optical thickness of four aerosol species collecting results of different transport models, concluded that sulfate aerosols are dominant in North America (about 70% of the total optical thickness). Their different result from observations could be caused by underestimation of carbonaceous aerosol concentrations in this region used in their estimation [*Liousse et al.*, 1996], as described in section 4.1. Therefore we conclude that the general understanding from previous studies that sulfate is a main anthropogenic aerosol should be modified. This conclusion also suggests that evaluation of anthropogenic aerosol effects on the climate system changes noticeably because optical characteristics of carbonaceous aerosols are different from those of sulfate aerosols.

Figure 8f shows the simulated and AVHRR-retrieved optical properties over the North Pacific without the AVHRR optical thickness because the satellite retrieval is not reliable for such small optical thicknesses. The simulated and observed Ångström exponents and the simulated optical thickness are larger in summertime, which suggests that a large amount of anthropogenic carbonaceous and sulfate aerosols are transported from China and Japan to the North Pacific regions, especially in summer. Figures 6 and 7 also show large transport of anthropogenic aerosols from North America and Europe to the North Atlantic in summertime. This large aerosol loading in summer may be attributed to the large oxidation of SO_2 and the strong vertical transport. The simulated optical thickness of sulfate aerosols is larger than that

Table 11. Comparison between Simulated and Observed SO_2 Concentrations

Location	Time Period	Concentration, pptv		Reference[a]
		Observation	Model	
Industrial regions, United States				
Indiana (40°N, 85°W)	annual	8530	2944	(a)
Kentucky (38°N, 88°W)	annual	7520	2637	(a)
Ohio (41°N, 82°W)	annual	7980	3201	(a)
Subarctic				
Cree Lake, Canada (58°N, 107°W)	annual	242	117	(b)
Ocean				
Amsterdam Island (38°N, 78°W)	annual	19	11	(c)
North Atlantic (48-37°N, 20°W)	Aug.	37	31	(d)
(38-7°N, 27-40°W)	Aug.	61	50	(d)
Equatorial Pacific (15°N-10°S, 145-165°W)	Feb. - March	28	52	(e)
Northeast Pacific (west of Seattle, United States)	April	28	16	(f)
Pacific (30-50°N, 170°W)	April - May	13	9	(g)
(15-29°N, 170°W)	April - May	82	30	(g)
(14°N-11°S, 170°W)	April - May	29	61	(g)

[a]Observed values: (a) *Shaw and Paur* [1983], (b) *Barrie and Bottenheim* [1990], (c) *Nguyen et al.* [1992], (d) *Pszenny et al.* [1990], (e) *Huebert et al.* [1993], (f) *Bandy et al.* [1992], and (g) *Quinn et al.* [1990].

Table 12. Comparison between Simulated and Observed Annual Mean Concentrations of Sulfate Aerosols

Location	Concentration, ng m^{-3}		Reference[a]
	Observation	Model	
Industrial regions, United States			
Albany, New York (42°N, 74°W)	6040	13792	(a)
Mayville, New York (42°N, 80°W)	5920	14272	(a)
Indiana (40°N, 85°W)	7400	10560	(b)
Kentucky (38°N, 88°W)	7400	7332	(b)
Ohio (41°N, 82°W)	6560	10560	(b)
Arctic and subarctic			
Alert, Canada (83°N, 61°W)	852	528	(c)
Bear Island, Norway (75°N, 19°E)	1408	1816	(d)
Cree Lake, Canada (58°N, 107°W)	768	1080	(e)
Heimaey, Iceland (64.40°N, 20.30°W)	636	956	(f)
Mould Bay, Canada (77°N, 119°W)	912	400	(g)
Ocean			
Barbados (13.17°N, 59.43°W)	816	1092	(h)
Bermuda (32.27°N, 64.87°W)	2336	1896	(h)
Mace Head (53.32°N, 9.85°W)	1288	1792	(h)
Cape Grim (40.68°S, 144.68°E)	380	408	(i)
Fanning (3.92°N, 159.33°W)	696	720	(j)
Midway Island (28.22°N, 177.35°W)	572	548	(j)
New Caledonia (22.15°S, 167.00°E)	448	928	(j)
Norfolk Island (29.08°S, 167.98°E)	300	720	(j)
Oahu (21.33°N, 157.70°W)	540	628	(j)
Antarctic			
Mawson (67.60°S, 62.50°E)	116	212	(k)
Palmer (64.77°S, 64.05°W)	100	188	(k)

[a]Observed values: (a) *Husain and Dutkiewicz* [1990], (b) *Shaw and Paur* [1983], (c) *Li and Barrie* [1993], (d) *Heintzenberg and Larssen* [1983], (e) *Barrie and Bottenheim* [1990], (f) *Prospero et al.* [1995], (g) *Barrie et al.* [1989], (h) *Galloway et al.* [1993], (i) *Ayers et al.* [1986], (j) *Savoie et al.* [1989], and (k) *Savoie et al.* [1993].

of carbonaceous aerosols affected by high DMS emissions and the promotion of chemical reactions in summer over such regions.

4.3.2. Soil dust regions. The column loading of soil dust aerosols is especially large around North Africa and the Middle and Near East. Over the Arabian Sea, soil dust aerosols are dominant from March to August, and the simulated and AVHRR-retrieved regional mean optical thicknesses reach about 0.5 in July (Figure 9a). Over the Saharan region the simulated optical thickness is higher from January to March, which is comparable to remote sensing values (Figures 9b and 9c). The simulated values are, however, underestimated in other months, which can be affected by a weaker surface wind velocity relatively than that in wintertime used in the model over the Saharan region. Such a small optical thickness is also recognized in results of other soil dust models as pointed out by *Tegen and Miller* [1998]. The small-scale convection, which is difficult to be modeled in the general circulation model, are very effective in generating dust storms, and therefore the transport model should be improved in this regard. In the Near East the polydispersion of the aerosol composition is simulated to have a characteristic aerosol variation, i.e., soil dust is dominant in spring, but anthropogenic aerosols (carbonaceous and sulfate aerosols) transported from Europe and an oil-producing region in the Middle East are noticeable from summer to fall (Figure 9d). This simulated seasonal variability corresponds to the seasonal variation of the AVHRR- and AERONET-measured Ångström exponents that are smaller in spring. Over soil dust regions affected by large particles, the simulated and observed Ångström exponents are smaller than that over industrial regions in general.

Satellite observations indicated that the location of the maximum optical thickness off the west coast of North Africa shifts seasonally [*Rao et al.*, 1988; *Moulin et al.*, 1997]; that is, the latitude of the maximum optical thickness is located around 10°N in January and around 20°N in July. There are several discussions about the mechanism of this seasonal shift. *Tegen and Fung* [1995] developed a three-dimensional model of soil dust aerosols using wind field calculated by a GCM with surface wind data of the European Centre for Medium-Range Weather Forecasts (ECMWF) and tried reproducing this seasonal shift. They could not reproduce this seasonal shift unless they introduced dust loading from disturbed soils in addition to those from natural sources. That is to say, they assumed larger emissions of anthropogenic soil dust aerosols originating from cultivation fields, so that the seasonal shift could be reproduced to some extent, although the location of the maximum optical thickness was not as low as 10°N in January. With the natural soil dust aerosols alone, our model also cannot explain this seasonal shift reasonably, especially the January position, in spite of realistic simulation using meteorological fields with the nudging technique. Simulated results for carbonaceous aerosols, however, produce a large optical thickness ($\approx$ 0.3) over this region in January. Thus we conclude that coexistence of natural soil dust from Sahara Desert and carbonaceous aerosols due to the biomass burning over the coast of the Gulf of Guinea well explains the mechanism of the seasonal shift (Figure 10). A large amount of carbonaceous

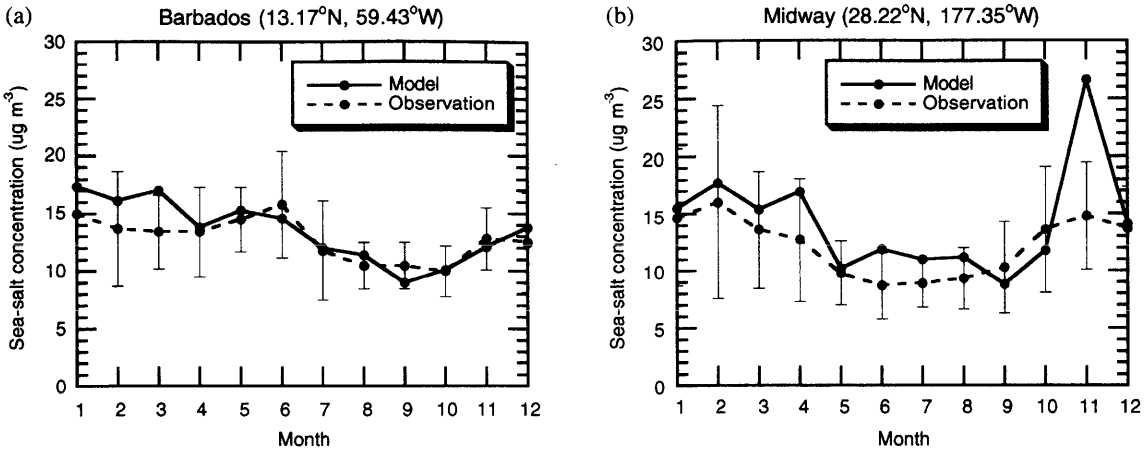

Figure 3. Comparisons between the simulated (solid lines) and the observed (dashed lines) monthly mean concentrations of sea-salt aerosols at (a) Barbados (13.17°N, 59.43°W) and (b) Midway (28.22°N, 177.35°W) in μg m^{-3}. The simulated concentrations are shown at the location for the observed values sited by *Tegen et al.* [1997].

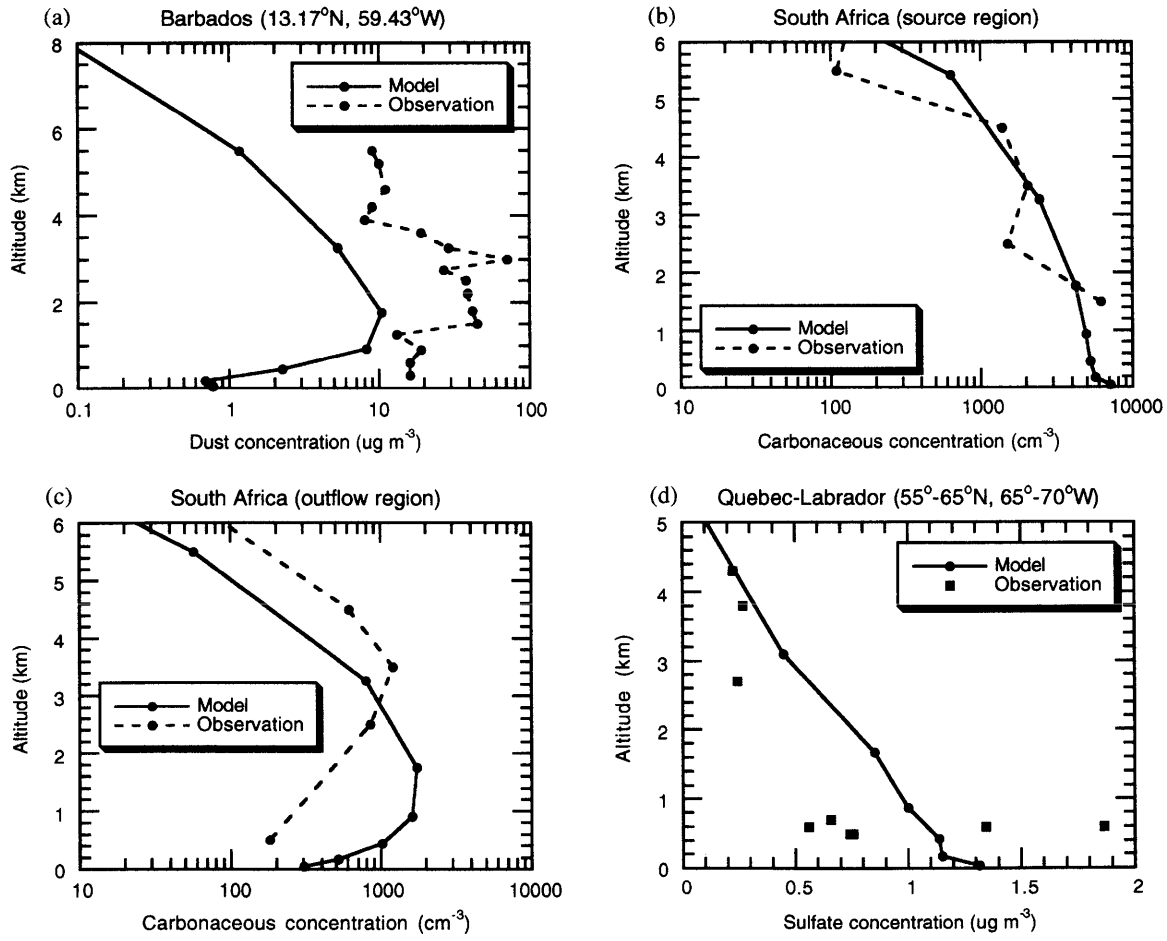

Figure 4. Vertical profiles of (a) soil dust aerosols at Barbados, carbonaceous aerosols over the (b) source and (c) outflow regions of biomass burning in the south of Africa, and (d) sulfate aerosols over the industrial region in Canada. Simulated monthly mean profiles (solid lines) for the corresponding locations and months are shown for the observed values (dashed lines or squares) in (a) July [*Prospero and Carlson*, 1972], (b, c) October [*Anderson et al.*, 1996], and (d) August [*Gorzelska et al.*, 1994].

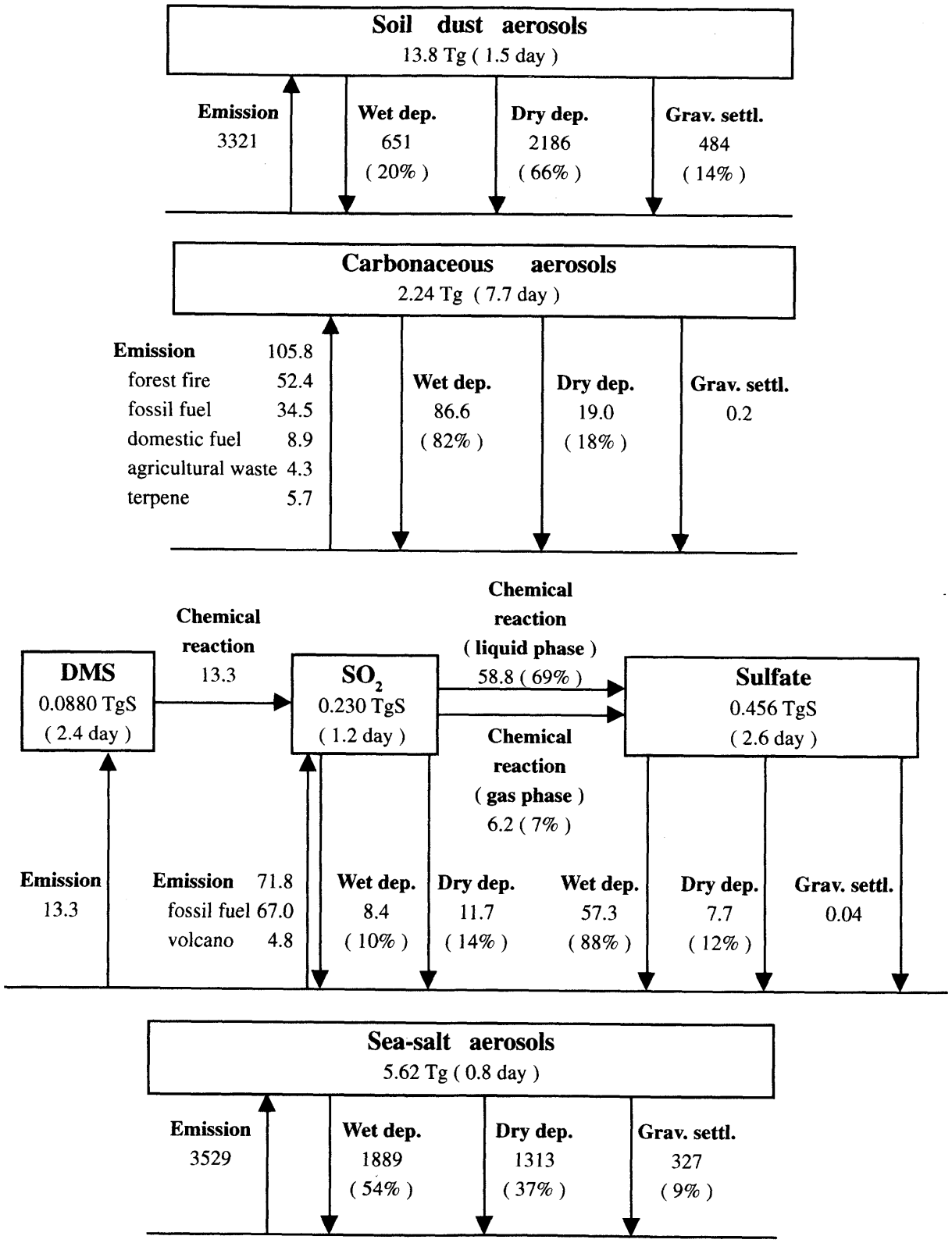

Figure 5. Global budgets of four aerosol species in the model. Emission, deposition, and oxidation fluxes are shown by arrows in Tg yr^{-1} (TgS yr^{-1} for sulfur cycle), and numbers in parentheses under each deposition and oxidation flux indicate the ratio to total fluxes. Annual mean global total loadings in Tg (TgS for sulfur cycle) and annual and global mean lifetimes in days in the atmosphere are indicated inside boxes.

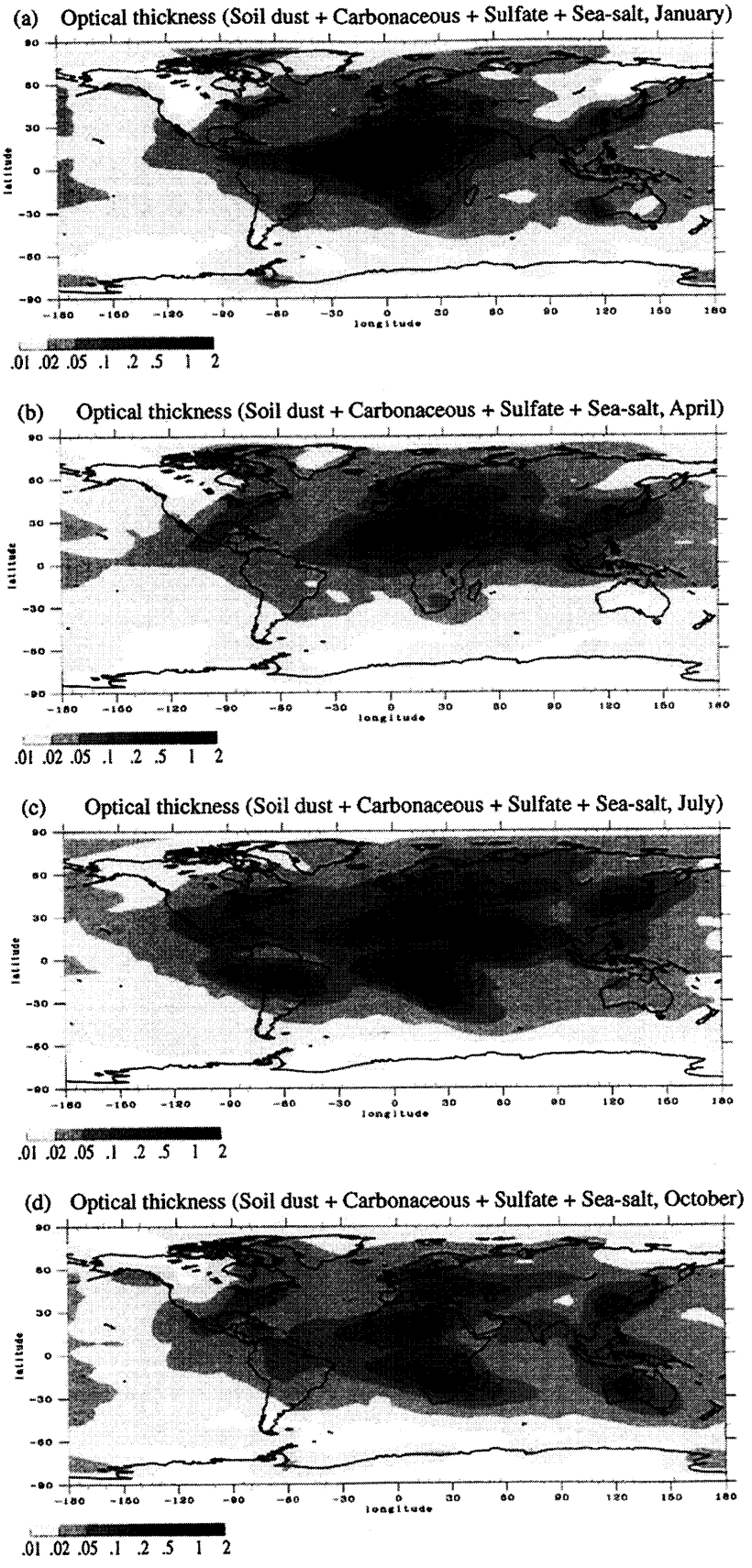

Figure 6. Monthly mean distributions of the simulated optical thickness for a mixed state of four aerosol species (soil dust, carbonaceous, sulfate, and sea salt) in (a) January, (b) April, (c) July, and (d) October.

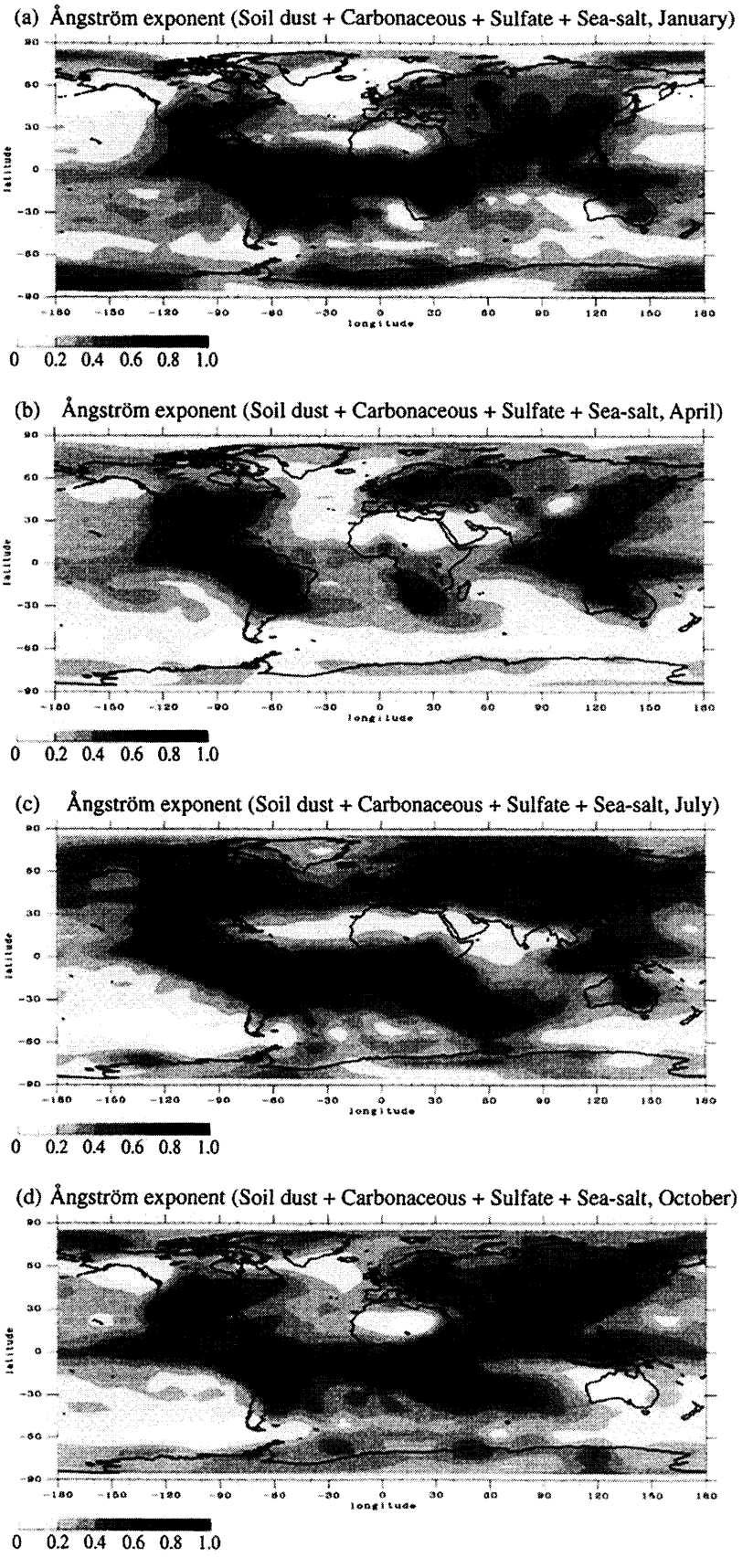

Figure 7. Monthly mean distributions of the simulated Ångström exponent for a mixed state of four aerosol species (soil dust, carbonaceous, sulfate, and sea salt) estimated from the optical thickness at the wavelengths of 0.55 μm and 1.0 μm in (a) January, (b) April, (c) July, and (d) October.

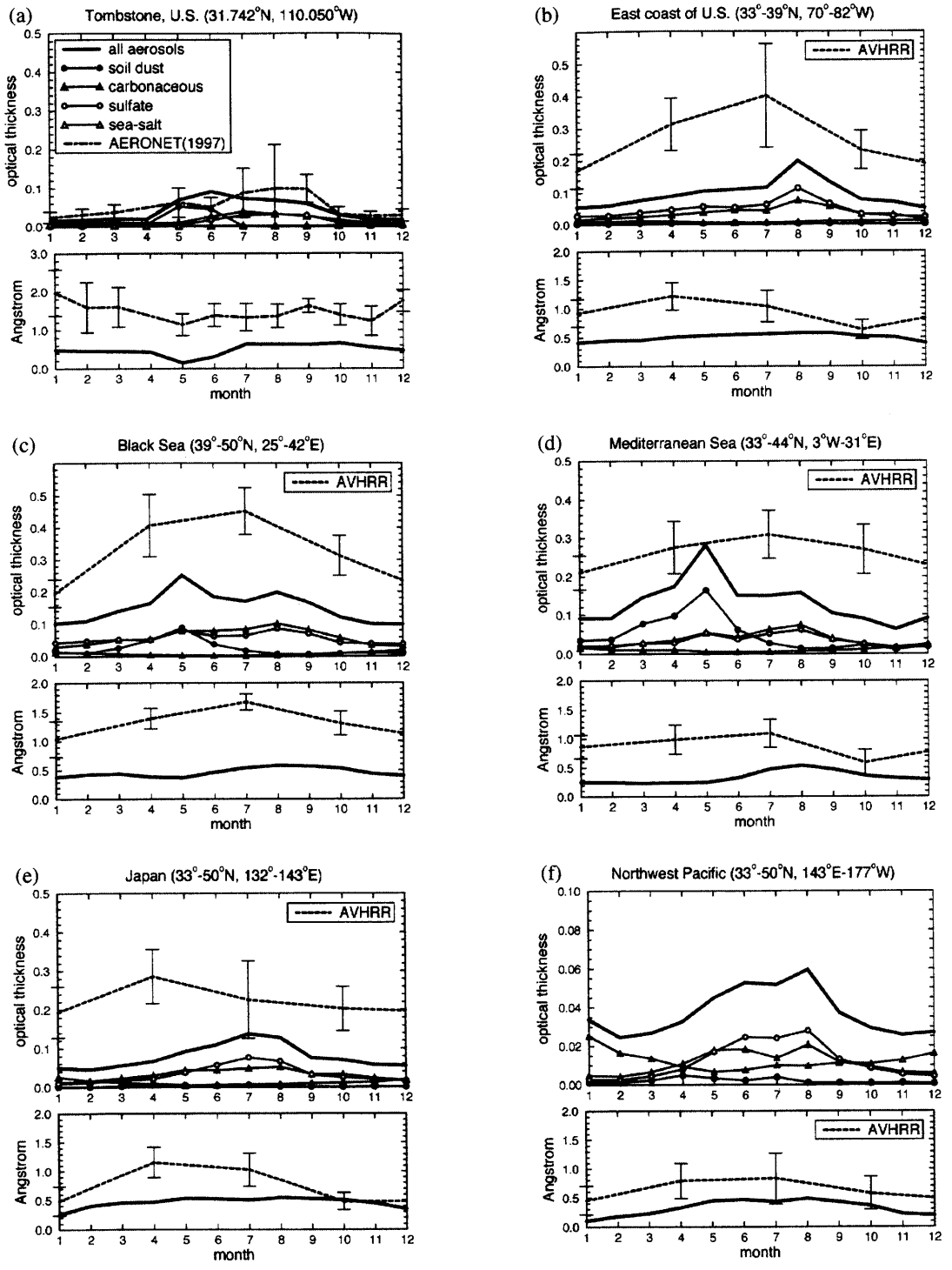

Figure 8. Seasonal variation of simulated and observed monthly mean optical thicknesses and Ångström exponents over industrial regions and remote ocean of midlatitudes of the Northern Hemisphere. The simulated optical thickness is shown for a mixed state of four aerosol species (solid line without symbols) and each aerosol type (solid lines with symbols). Observed optical thickness and Ångström exponent from AVHRR (dashed lines) and from AERONET (dashed-dotted lines) are also shown with standard deviations.

aerosols originating from biomass burning was observed in a savanna region along the Gulf of Guinea in January [*Cachier et al.*, 1991], and the strong radiative forcing of carbonaceous aerosols in this region has been estimated by *Hansen et al.* [1998] and *Penner et al.* [1998].

4.3.3. Biomass burning regions. Biomass burning regions concentrate in the Southern Hemisphere as mentioned in section 4.1. Figure 11a indicates a mixed state of carbonaceous and soil dust aerosols over the coast of the Gulf of Guinea from January to June described in section 4.3.2. In other seasons the large optical thickness is affected by biomass burning over the south of Africa. Figures 11b, 11c, and 11d show biomass burning over the south of Africa. The simulated optical thickness is a little different from the AVHRR values within 30% in the biomass

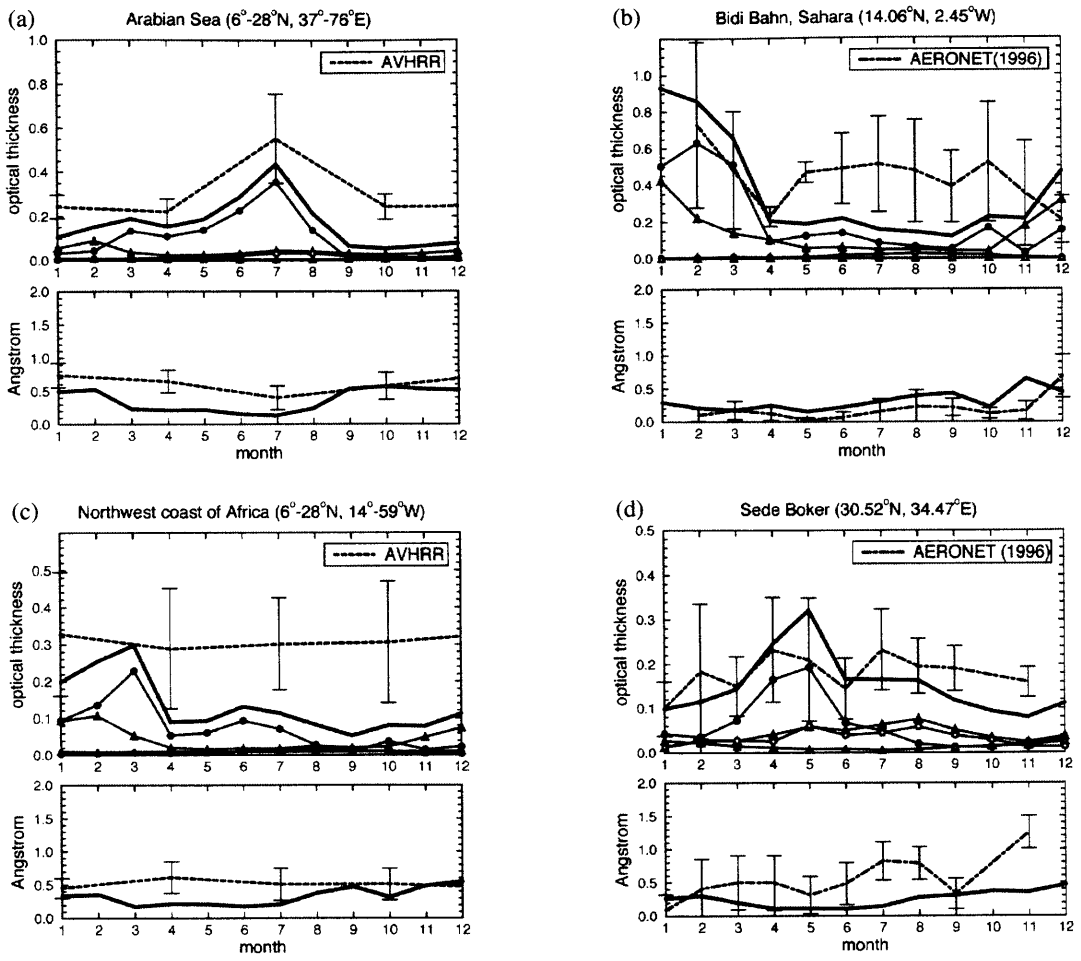

Figure 9. Same as Figure 8 but for soil dust regions.

burning season, though there is a large difference in other seasons. It should be noted that the AVHRR retrieval becomes unreliable for such small optical thicknesses as less than 0.2 because the retrieval is sensitive to assumptions of atmospheric components and calibration constants in weak radiance [*Higurashi and Nakajima*, 1999].

5. Conclusion

In this study we developed the three-dimensional global aerosol climate model that can treat various species of aerosols and validated it using satellite data, i.e., AVHRR retrievals, and ground-based optical remote sensing data, such as AERONET. This model treats major components of tropospheric aerosols such as soil dust, carbonaceous (organic and black carbon), sulfate, and sea-salt particles, by introducing various physical processes of the emission, advection, diffusion, wet deposition (subcloud and in-cloud scavengings), dry deposition, and gravitational settling. Chemical reactions and solubility of precursor gases are also included for sulfate aerosols. The combined optical thickness and Ångström exponent, due to four aerosol species, are also calculated to evaluate the radiative effect of aerosols on climate and to compare with remote sensing data. The necessary meteorological parameters in this model are prepared by means of the nudging technique using NCEP/NCAR reanalysis data. The uplift scheme using the surface temperature and the potential temperature is incorporated to represent instability of the atmosphere, which is necessary to reproduce vertical profiles of aerosols. Then the wind velocity with an altitude of 10 m is calculated for those of soil dust and sea-salt aerosols from these meteorological parameters. The GEIA and FAO databases are used for estimation of emission fluxes of carbonaceous aerosols and sulfur species.

The global distributions of the simulated optical thickness and Ångström exponent in a mixed state of major four aerosol species is then compared with AVHRR retrievals, and they are generally in good agreement. The large optical thickness of soil dust aerosols has been reproduced over Saharan and Arabian regions as shown by the AVHRR retrievals. Characteristic distributions of the optical thickness of carbonaceous aerosols have been simulated for the sources in the center and south of Africa and Amazon during the dry season. The results have suggested that the seasonal shift of the aerosol optical thickness peak off the west coast of North Africa is caused by coexistence of soil dust and carbonaceous aerosols in January around 10°N. The comparable contributions of anthropogenic carbonaceous and sulfate aerosols to the total optical thickness are successfully simulated in midlatitudes of the Northern Hemisphere, which agrees with recent observations. The simulated optical thickness and Ångström exponent over the remote ocean of midlatitudes of the Northern Hemisphere also have suggested the large transport of anthropogenic aerosols from industrial regions.

We still have several aspects to improve our model. For instance, the global distributions of various species of aerosols have

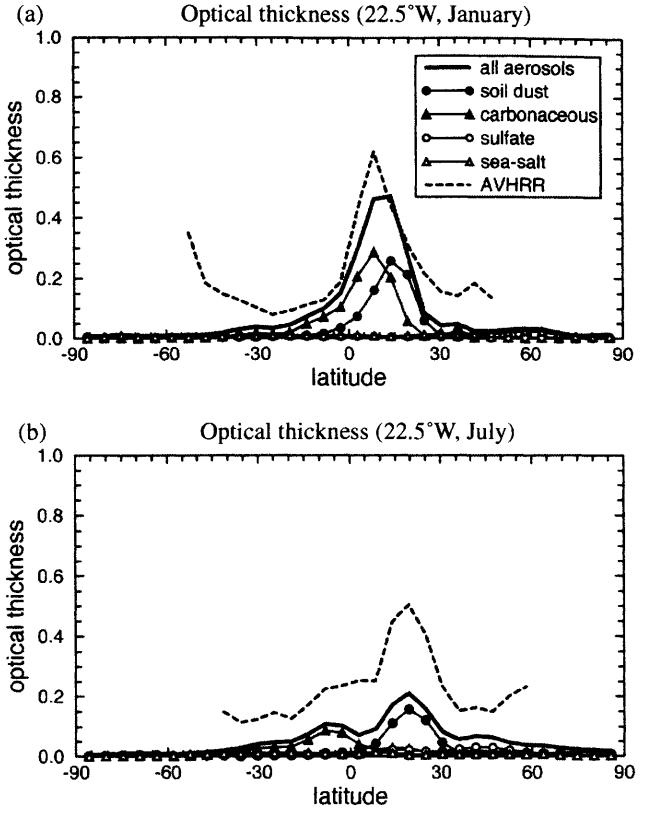

Figure 10. Comparison between simulated (solid lines) and AVHRR (dashed line) optical thicknesses along 22.5°W in (a) January and (b) July.

to be simulated without the nudging technique because it is important to simulate aerosol distributions in the future climate; an improvement of sulfur chemistry will be important for the future climate simulation. It is also useful to implement prognostic schemes of generating industrial and biomass burning materials with model parameters. Incorporation of indirect effect of aerosols is necessary, yet requires the detail knowledge about the mechanism [e.g., *Facchini et al.*, 1999].

Appendix A: Emission, Diffusion, and Deposition Processes

Vertical uplift levels of aerosols at the emission are mainly decided using the potential temperature of each layer and the surface temperature in this model. Aerosols are emitted with the constant mixing ratio from the lowest model layer to the layer whose potential temperature is lower than the surface temperature,

$$q_a = q_{ao} + \frac{F_E g \Delta t}{p_0 - p_{\theta<Ts}}, \tag{A1}$$

where q_{ao} is the aerosol mixing ratio before the time step, g is the gravitational constant, Δt is the model time step, p_0 is the surface pressure, and $p_{\theta<Ts}$ is the pressure at the highest layer whose potential temperature is lower than the surface temperature. It is expected by using this emission scheme to increase the total aerosol mass in the atmosphere in summertime and also to reproduce the diurnal variability of the emission height. However, the treatment of carbonaceous aerosols originating from forest fires is different because the uplift mechanism of forest fires depends also on the fire temperature and the burned area which are difficult to be evaluated in the AGCM. The aerosol emission from forest fires therefore occurs in the first six layers (below about 3 km) with a constant mixing ratio in this model according to several observations [*Kaufman et al.*, 1992; *Browell et al.*, 1996].

The vertical diffusion flux F_D is calculated as follows:

$$F_D = -\rho_{air} K \frac{\partial q_a}{\partial z}, \tag{A2}$$

where K is the diffusion coefficient. The present model also takes into consideration a simple shallow convection using the saturated specific humidity q^* and the humid static energy h. If the following formulae are satisfied,

$$h_k > h^*_{k+1}, \tag{A3}$$

$$q^*_w(T') < q_{w,k} \qquad \left(T' = \frac{h_k - g z_{k+1} - L q_{w,k}}{C_p}\right), \tag{A4}$$

where k is the model layer number, h^* is the saturated humid static energy, q_w is the specific humidity, L is the latent heat of evaporation for water, and C_p is the atmospheric specific heat of constant pressure, aerosol mixing ratios of the kth and k+1th layers are given as same.

The deposition of aerosols is roughly divided into three processes: i.e., wet deposition, dry deposition, and gravitational settling. The wet deposition is also divided into two processes; one is the sub-cloud scavenging that raindrops collide with aerosol particles due to the different dropping velocities. The change rate of the aerosol number concentration with the sub-cloud scavenging ΔN_{ar} is evaluated as

$$\Delta N_{ar} = E\pi(r_r + r_a)^2 (v_r - v_a) N_r N_a, \tag{A5}$$

where E is the collision efficiency depending on aerosol particle and raindrop radii according to *Grover and Pruppacher* [1985], r_r and r_a are raindrop and aerosol radii, respectively, N_r and N_a are number concentrations of raindrops and aerosol particles, and v_r and v_a are respective terminal velocities. Values v_a follow the Stokes' law,

$$v_a = \frac{2\rho_a r_a^2 g}{9\eta}, \tag{A6}$$

where ρ_a is the density of aerosol particles shown in section 3, and η is the viscosity of air assumed to be 1.78×10^{-5} kg m^{-1} s^{-1}. The raindrop radius r_r is chosen as 500 μm and v_r as 0.5 m s^{-1} in this model. Then the aerosol mass flux with the sub-cloud scavenging F_{co} is estimated as

$$F_{co} = -m_a \Delta N_{ar} \Delta z_k, \tag{A7}$$

where m_a is the aerosol particle mass and Δz_k is the geometrical thickness of the kth layer. The other wet deposition process is the in-cloud scavenging that aerosol particles in cloud water are removed from the atmosphere by precipitation. The formula for the in-cloud scavenging is given as follows:

$$q_{a,d} = \frac{R_n}{R_n + C_w} C_{in} C_f q_a, \tag{A8}$$

where $q_{a,d}$ is the aerosol mixing ratio in raindrops, R_n is the new rain formation, C_w is the cloud water, C_{in} is the ratio of aerosols in cloud water to the total aerosols (the in-cloud coefficient), and C_f is the cloud fraction. C_{in} of sulfate aerosols is assumed to be 0.6 based on some measurements [*Boucher and Lohmann*, 1995] in this model. Other aerosol species are, however, not as hydrophilic as sulfate aerosols, so that C_{in} is assumed to be 0.3 for carbona-

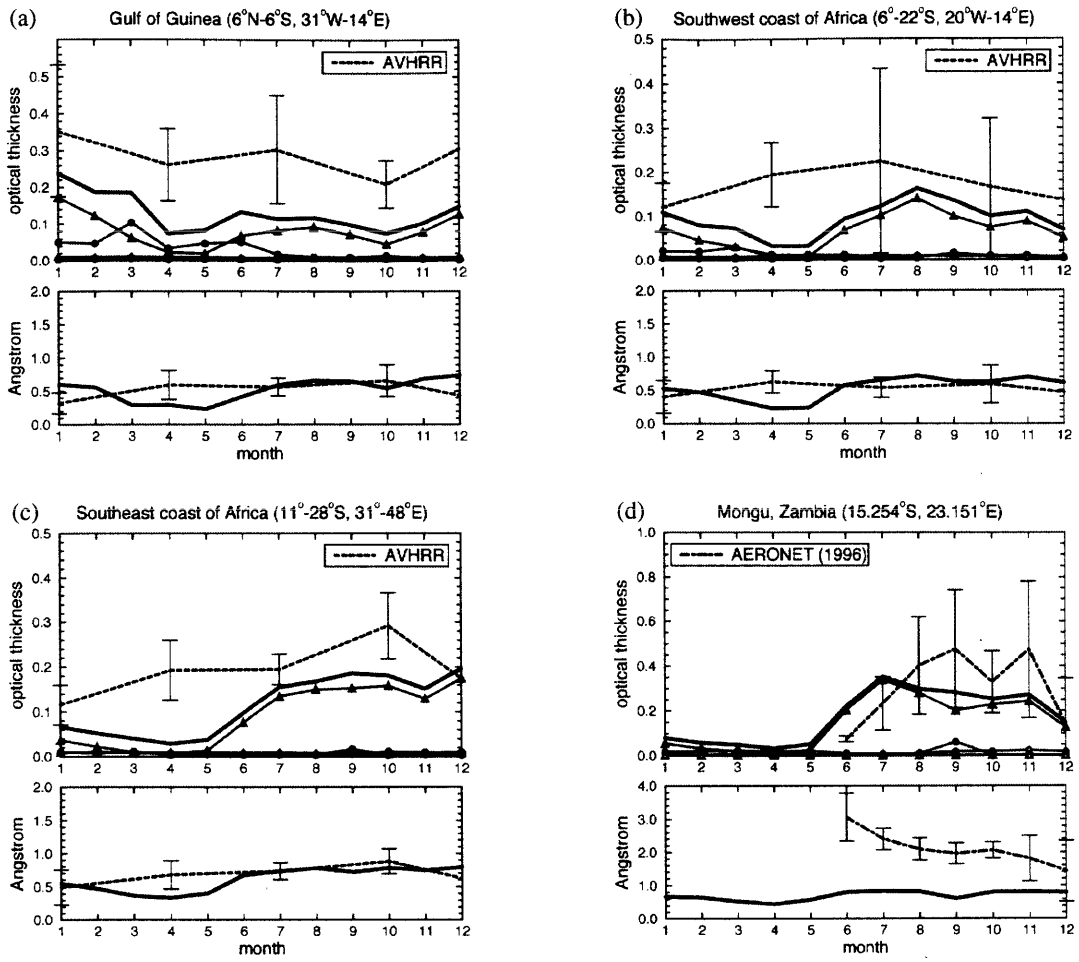

Figure 11. Same as Figure 8 but for biomass burning regions.

ceous and sea-salt aerosols, 0.1 for soil-dust aerosols, respectively. Therefore the in-cloud scavenging flux F_{in} is given as

$$F_{in} = -\rho_{\text{air}} \frac{q_{a,d}}{\Delta t} \Delta z_k . \tag{A9}$$

This model also has a reemission process of aerosols with evaporation of raindrops. This process occurs in the condition that the precipitation flux at the upper boundary of each model layer $F_r(k+1/2)$ is lager than that at the lower boundary $F_r(k-1/2)$. The aerosol mass flux with evaporation of rain drops F_{ae} at the kth layer is given as follows:

$$F_{ae} = -\frac{F_r(k+1/2) - F_r(k-1/2)}{F_r(k+1/2)} \sum_{l=k}^{k_{\max}} \left(F_{co}(l) + F_{in}(l) \right), \tag{A10}$$

The dry deposition is caused by turbulent mixing with a flux F_{dry} given as,

$$F_{\text{dry}} = -\rho_{\text{air}} \frac{v_{\text{dry}} |\mathbf{v}_{k=1}| C_d}{v_{\text{dry}} + |\mathbf{v}_{k=1}| C_d} q_a , \tag{A11}$$

where v_{dry} is the dry deposition velocity introduced for carbonaceous and sulfate aerosols, $|\mathbf{v}_{k=1}|$ is the wind velocity at the first model layer, and C_d is the balk coefficient. Value v_{dry} is set as 0.1 cm s^{-1} for carbonaceous aerosols, 0.2 cm s^{-1} for sulfate, and 0.8 and 0.6 cm s^{-1} for SO_2 over ocean and land, respectively. The mass flux with gravitational settling is given as

$$F_g = -\rho_{\text{air}} v_a , \tag{A12}$$

Finally, the deposition flux F_S is calculated as follows:

$$F_S = F_{co} + F_{in} + F_{ae} + F_{\text{dry}} + F_g . \tag{A13}$$

Appendix B: Calculation of Optical Thickness

The optical thickness τ at a wavelength of 0.55 μm is calculated at each time step in this model with the formula

$$\tau = \sum_i \left(\frac{3}{4} \sum_{k=1}^{k_{\max}} \frac{Q_{\text{ext}}(i,k) q_a(i,k) \Delta p_k}{\rho_a(k) r_{\text{eff}}(i,k) g} \right), \tag{B1}$$

Table 13. Effective Radius of Carbonaceous and Sulfate Aerosols Used in the Calculation of the Optical Thickness

Radius Range, μm	Effective Radius, μm
0.0100 – 0.0158	0.0126
0.0158 – 0.0251	0.0200
0.0251 – 0.0398	0.0316
0.0398 – 0.0631	0.0501
0.0631 - 0.100	0.0794
0.100 - 0.158	0.126
0.158 - 0.251	0.200
0.251 – 0.398	0.316
0.398 - 0.631	0.501
0.631 - 1.00	0.794

where $Q_{ext}(i,k)$ is the extinction efficiency factor as a function of the particle size bin i, aerosol type, and relative humidity for each grid k, r_{eff} is the effective radius of the aerosol particle, and Δp_k is the pressure difference between the upper and the lower boundaries at the kth layer. The Mie theory is used to determine the extinction efficiency factor. The lognormal size distribution is assumed for carbonaceous and sulfate aerosols in the calculation of the optical thickness, and the effective radius is shown in Table 13. The standard deviations are set as 1.55 for carbonaceous aerosols [*Martins et al.*, 1996] and 2.03 for sulfate aerosols [*d'Almeida et al.*, 1991]. The mode radius of the lognormal distribution is taken into consideration for the growth of particles by absorbing water as a function of the relative humidity same as transport processes (Tables 2 and 3). Refractive indices of these aerosols used in the calculation of the extinction efficiency factor for each effective radius are volume-weighted with water [*Shettle and Fenn*, 1979],

$$m = m_w + (m_o - m_w)\left(\frac{r_o}{r_m}\right)^3, \qquad \text{(B2)}$$

where m_o and m_w are refractive indices of the dry aerosol and water, respectively, r_o is the dry aerosol radius, and r_m is the mode radius depending on the relative humidity. Value r_o is assumed as 0.18 μm for carbonaceous aerosols [*Martins et al.*, 1996] and 0.139 μm for sulfate aerosols [*d'Almeida et al.*, 1991]. The volume-weighted refractive index is also used for the internal mixture of BC and OC. Value m_o is set as $1.53\text{-}6.00\times10^{-3}i$ for OC, $1.75\text{-}0.440i$ for BC, $1.43\text{-}1.00\times10^{-8}i$ for sulfate, and m_w as $1.33\text{-}1.96\times10^{-9}i$ for water [*d'Almeida et al.*, 1991]. In the case of soil dust and sea-salt aerosols, the same size distribution and the effective radius are used as in the transport processes described in sections 3.1 and 3.4. Refractive indices are assumed as $1.53\text{-}5.50\times10^{-3}i$ for soil dust and $1.38\text{-}3.70\times10^{-9}i$ for sea-salt aerosols, respectively.

Acknowledgments. The authors are grateful to B. N. Holben for providing AERONET data for validation. The study was supported by the Grant-in-Aid for Scientific Research on Priority Areas (10304035) of the Japanese Ministry of Education, Science, Sports, and Culture.

References

Anderson, B. E., W. B. Grant, G. L. Gregory, E. V. Browell, J. E. Collins Jr., G. W. Sachse, D. R. Bagwell, C. H. Hudgins, D. R. Blake, and N. J. Blake, Aerosols from biomass burning over the tropical South Atlantic region: Distributions and impacts, *J. Geophys. Res.*, *101*, 24,117-24,137, 1996.

Andreae, M. O., Global distribution of fires seen from space, *EOS, Trans. Amer. Geophys. Union*, *74*, 129-135, 1993.

Andreae, M. O., R. J. Ferek, F. Bermond, K. P. Byrd, R. T. Engstrom, S. Hardin, P. D. Houmere, F. LeMarrec, and H. Raemdonck, Dimethyl sulfide in the marine atmosphere, *J. Geophys. Res.*, *90*, 12,891-12,900, 1985.

Andres, R. J., and A. D. Kasgnoc, A time-averaged inventory of subaerial volcanic sulfur emissions, *J. Geophys. Res.*, *103*, 25,251-25,261, 1998.

Ayers, G. P., J. P. Ivey, and H. S. Goodman, Sulfate and methanesulfonate in the maritime aerosol at Cape Grim, Tasmania, *J. Atmos. Chem.*, *4*, 173-185, 1986.

Bandy, A. R., D. L. Scott, B. W. Blomquist, S. M. Chen, and D. C. Thornton, Low yields of SO_2 from dimethyl sulfide oxidation in the marine boundary layer, *Geophys. Res. Lett.*, *19*, 1125-1127, 1992.

Barrie, L. A., and J. W. Bottenheim, Sulphur and nitrogen pollution in the arctic atmosphere, in *Pollution of the Arctic Atmosphere*, edited by W. T. Sturges, pp. 158-181, Elsevier, New York, 1990.

Barrie, L. A., M. P. Olson, and K. K. Oikawa, The flux of anthropogenic sulphur into the arctic from mid-latitudes in 1979/80, *Atmos. Environ.*, *23*, 2505-2515, 1989.

Bates, T. S., R. J. Charlson, and R. H. Gammon, Evidence for the climate role of marine biogenic sulphur, *Nature*, *329*, 319-321, 1987.

Benkovitz, C. M., M. T. Scholtz, J. Pacyna, L. Tarrasón, J. Dignon, E. C. Voldner, P. A. Spiro, J. A. Logan, and T. E. Graedel, Global gridded inventories of anthropogenic emissions of sulfur and nitrogen, *J. Geophys. Res.*, *101*, 29,239-29,253, 1996.

Bodhaine, B. A., Aerosol absorption measurements at Barrow, Mauna Loa, and the south pole, *J. Geophys. Res.*, *100*, 8967-8975, 1995.

Boucher, O., and U. Lohmann, The sulfate-CCN-cloud albedo effect, *Tellus, Ser. B*, *47*, 281-300, 1995.

Browell, E. V., et al., Ozone and aerosol distributions and air mass characteristics over the South Atlantic Basin during the burning season, *J. Geophys. Res.*, *101*, 24,043-24,068, 1996.

Cachier, H., P. Buat-Ménard, M. Fontugne, and R. Chesselet, Long-range transport of continentally-derived particulate carbon in the marine atmosphere: Evidence from stable carbon isotope studies, *Tellus, Ser. B*, 38, 161-177, 1986.

Cachier, H., J. Ducret, M. P. Brémond, V. Yoboué, J. P. Lacaux, A. Gaudichet, and J. Baudet, Biomass burning aerosols in a savanna region of the Ivory Coast, in *Global Biomass Burning*, edited by J. S. Levine, pp. 174-180, MIT Press, Cambridge, Mass., 1991.

Cahoon, D. R., Jr., B. J. Stocks, J. S. Levine, W. R. Cofer III, and K. P. O'Neill, Seasonal distribution of African savanna fires, *Nature*, *359*, 812-815, 1992.

Chameides, W. L., The photochemistry of a remote marine stratiform cloud, *J. Geophys. Res.*, *89*, 4739-4755, 1984.

Charlson, R. J., S. E. Schwartz, J. M. Hales, R. D. Cess, J. A. Coakley Jr., J. E. Hansen, and D. J. Hofmann, Climate forcing by anthropogenic aerosols, *Science*, *255*, 423-430, 1992.

Chatfield, R. B., and P. J. Crutzen, Are there interactions of iodine and sulfur species in marine air photochemistry?, *J. Geophys. Res.*, *95*, 22,319-22,341, 1990.

Chin, M., D. J. Jacob, G. M. Gardner, M. S. Foreman-Fowler, and P. A. Spiro, A global three-dimensional model of tropospheric sulfate, *J. Geophys. Res.*, *101*, 18,667-18,690, 1996.

Cooke, W. F., and J. J. N. Wilson, A global black carbon aerosol model, *J. Geophys. Res.*, *101*, 19,395-19,409, 1996.

d'Almeida, G. A., and L. Schütz, Number, mass and volume distributions of mineral aerosol and soils of the Sahara, *J. Clim. Appl. Meteorol.*, *22*, 233-243, 1983.

d'Almeida, G. A., P. Koepke, and E. P. Shettle, *Atmospheric Aerosols: Global Climatology and Radiative Characteristics*, 561 pp., A. Deepak, Hampton, Virginia, 1991.

da Silva, A., A. C. Young, and S. Levitus, Atlas of surface marine data 1994, vol. 1, Algorithms and procedures, in *NOAA Atlas NESDIS*, vol. 6, U.S. Dep. of Comm., Washington, D. C., 1994.

DeFries, R. S., and J. R. G. Townshend, NDVI-derived land cover classifications at a global scale, *Int. J. Remote Sens.*, *15*, 3567-3586, 1994.

DeMore, W. B., S. P. Sander, D. M. Golden, R. F. Hampson, M. J. Kurylo, C. J. Howard, A. R. Ravishankara, C. E. Kolb, and M. J. Molina, Chemical kinetics and photochemical data for use in stratospheric modeling, *JPL Publ. 97-4*, 266 pp., Jet Propul. Lab., Pasadena, Calif., 1997.

Dentener, F. J., G. R. Carmichael, Y. Zhang, J. Lelieveld, and P. J. Crutzen, Role of mineral aerosol as reactive surface in the global troposphere, *J. Geophys. Res.*, *101*, 22,869-22,889, 1996.

Erickson, D. J., and R. A. Duce, On the global flux of atmospheric sea salt, *J. Geophys. Res.*, *93*, 14,079-14,088, 1988.

Erickson, D. J., J. T. Merrill, and R. A. Duce, Seasonal estimates of global atmospheric sea-salt distribution, *J. Geophys. Res.*, *91*, 1067-1072, 1986.

Facchini, M. C., M. Mircea, S. Fuzzi, and R. J. Charlson, Cloud albedo enhancement by surface-active organic solutes in growing droplets, *Nature*, *401*, 257-259, 1999.

FAO, FAO yearbook of forest products, *FAO Statistics Series*, 376 pp., Food and Agric. Organ. of the United Nations, Rome, 1995a.

FAO, FAO production yearbook, *FAO Statistics Series*, 244 pp., Food and Agric. Organ. of the United Nations, Rome, 1995b.

FAO, *State of the World's Forests*, 201 pp., Food and Agric. Organ. of the United Nations, Rome, 1997.

Feichter, J., E. Kjellstrom, H. Rodhe, F. Dentener, J. Lelieveld, and G. J. Roelofs, Simulation of the tropospheric sulfur cycle in a global climate model, *Atmos. Environ.*, *30*, 1693-1708, 1996.

Galloway, J. N., D. L. Savoie, W. C. Keene, and J. M. Prospero, The temporal and spatial variability of scavenging ratios for nss-sulfate, nitrate, methanesulfonate and sodium in the atmosphere over the North Atlantic Ocean, *Atmos. Environ., Ser. A*, 27, 235-250, 1993.

Gillette, D., A wind tunnel simulation of the erosion of soil: Effect of soil texture, sandblasting, wind speed, and soil consolidation on dust production, *Atmos. Environ.*, *12*, 1735-1743, 1978.

Gorzelska, K., R. W. Talbot, K. Klemm, B. Lefer, O. Klemm, G. L. Gregory, B. Anderson, and L. A. Barrie, Chemical composition of the atmospheric aerosol in the troposphere over the Hudson Bay lowlands and Quebec-Labrador regions of Canada, *J. Geophys. Res.*, *99*, 1763-1779, 1994.

Grover, S. N., and H. R. Pruppacher, The effect of vertical turbulent fluctuations in the atmosphere on the collision of aerosol particles by cloud drops, *J. Atmos. Sci.*, *34*, 2305-2318, 1985.

Guenther, A., et al., A global model of natural volatile organic compound emissions, *J. Geophys. Res.*, *100*, 8873-8892, 1995.

Hänel, G., The properties of atmospheric aerosol particles as functions of the relative humidity at thermodynamic equilibrium with the surrounding moist air, *Adv. Geophys.*, *19*, 73-188, 1976.

Hansen, J. E., M. Sato, A. Lacis, R. Ruedy, I. Tegen, and E. Matthews, Climate forcing in the industrial era, *Proc. Natl. Acad. Sci.*, *95*, 12,753-12,758, 1998.

Hegg, D. A., J. Livingston, P. V. Hobbs, T. Novakov, and P. Russell, Chemical apportionment of aerosol column optical depth off the mid-Atlantic coast of the United States, *J. Geophys. Res.*, *102*, 25,293-25,303, 1997.

Heintzenberg, J., and S. Larssen, SO_2 and SO_4^{2-} in the arctic: Interpretation of observations at three Norwegian arctic-subarctic stations, *Tellus, Ser. B*, 35, 255-265, 1983.

Heintzenberg, J., K. Müller, W. Birmili, G. Spindler, and A. Wiedensohler, Mass-related aerosol properties over the Leipzig basin, *J. Geophys. Res.*, *103*, 13,125-13,135, 1998.

Herman, J. R., P. K. Bhartia, O. Torres, C. Hsu, C. Seftor, and E. Celarier, Global distributions of UV-absorbing aerosols from Nimbus 7/TOMS data, *J. Geophys. Res.*, *102*, 16,911-16,923, 1997.

Higurashi, A., and T. Nakajima, Development of a two-channel aerosol retrieval algorithm on a global scale using NOAA AVHRR, *J. Atmos. Sci.*, *56*, 924-941, 1999.

Higurashi, A., T. Nakajima, B. N. Holben, A. Smirnov, R. Frouin, and B. Chatenet, A study of global aerosol optical climatology with two channel AVHRR remote sensing, *J. Clim.*, in press, 1999.

Hobbs, P. V., J. S. Reid, R. A. Kotchenruther, R. J. Ferek, and R. Weiss, Direct radiative forcing by smoke from biomass burning, *Science*, *275*, 1776-1778, 1997.

Hoffman, E. J., and R. A. Duce, Organic carbon in marine atmospheric particulate matter: Concentration and particle size distribution, *Geophys. Res. Lett.*, *4*, 449-452, 1977.

Holben, B. N., et al., AERONET—A federated instrument network and data archive for aerosol characterization, *Remote Sens. Environ.*, *66*, 1-16, 1998.

Horvath, H., Atmospheric light absorption—A review, *Atmos. Environ., Ser. A*, *27*, 293-317, 1993.

Huebert, B. J., S. Howell, P. Laj, J. E. Johnson, T. S. Bates, P. K. Quinn, V. Yegorov, A. D. Clarke, and J. N. Porter, Observations of the atmospheric sulfur cycle on SAGA3, *J. Geophys. Res.*, *98*, 16,985-16,995, 1993.

Husain, L., and V. A. Dutkiewicz, A long-term (1975-1988) study of atmospheric SO_4^{2-}: Regional contributions and concentration trends, *Atmos. Environ., Ser. A*, *24*, 1175-1187, 1990.

Hynes, A. J., P. H. Wine, and D. H. Semmes, Kinetics and mechanism of OH reactions with organic sulfides, *J. Phys. Chem.*, *90*, 4148-4156, 1986.

Intergovernmental Panel on Climate Change (IPCC), *Climate Change 1995: The Science of Climate Change*, J. T. Houghton, L. G. Meira Filho, B. A. Callander, N. Harris, A. Kattenberg, and K. Maskell (Eds.), 572 pp., Cambridge Univ. Press, New York, 1996.

Joussaume, S., Three-dimensional simulations of the atmospheric cycle of desert dust particles using a general circulation model, *J. Geophys. Res.*, *95*, 1909-1941, 1990.

Kalma, J. D., J. G. Speight, and R. J. Wasson, Potential wind erosion in Australia: A continental perspective, *J. Climatol.*, *8*, 411-428, 1988.

Kaufman, Y. J., A. Setzer, D. Ward, D. Tanre, B. N. Holben, P. Menzel, M. C. Pereira, and R. Rasmussen, Biomass burning airborne and spaceborne experiment in the Amazonas (BASE-A), *J. Geophys. Res.*, *97*, 14,581-14,599, 1992.

Kneizys, F. X., E. P. Shettle, G. P. Anderson, L. W. Abreu, J. H. Chetwynd, J. E. A. Selby, S. A. Clough, and W. O. Gallery, LOWTRAN 7 Revision 4.0, Air Force Geophys. Lab., Bedford, Mass., 1990.

Langner, J., and H. Rodhe, A global three-dimensional model of the tropospheric sulfur cycle, *J. Atmos. Chem.*, *13*, 225-263, 1991.

Lee, G., J. T. Merrill, and B. J. Huebert, Variation of free tropospheric total nitrate at Mauna Loa Observatory, Hawaii, *J. Geophys. Res.*, *99*, 12,821-12,831, 1994.

Li, S. M., and L. A. Barrie, Biogenic sulfur aerosol in the Arctic troposphere, 1, Contributions to total sulfate, *J. Geophys. Res.*, *98*, 20,613-20,622, 1993.

Li, X., H. Maring, D. Savoie, K. Voss, and J. M. Prospero, Dominance of mineral dust in aerosol light-scattering in the North Atlantic trade winds, *Nature*, *380*, 416-419, 1996.

Liousse, C., J. E. Penner, C. Chuang, J. J. Walton, H. Eddleman, and H. Cachier, A global three-dimensional model study of carbonaceous aerosols, *J. Geophys. Res.*, *101*, 19,411-19,432, 1996.

Louis, J., A parametric model of vertical eddy fluxes in the atmosphere, *Boundary Layer Meteorol.*, *17*, 187-202, 1979.

Malm, W. C., J. F. Sisler, D. Huffman, R. A. Eldred, and T. A. Cahill, Spatial and seasonal trends in particle concentration and optical extinction in the United States, *J. Geophys. Res.*, *99*, 1347-1370, 1994.

Martins, J. V., P. Artaxo, P. V. Hobbs, C. Liousse, H. Cachier, Y. Kaufman, and A. Plana-Fattori, Particle size distributions, elemental compositions, carbon measurements, and optical properties of smoke from biomass burning in the Pacific Northwest of the United States, in *Biomass Burning and Global Change*, vol. 2, edited by J. S. Levine, pp. 716-732, MIT Press, Cambridge, Mass., 1996.

Matthews, E., Global vegetation and land use: New high-resolution data bases for climate studies, *J. Clim. Appl. Meteorol.*, *22*, 474-487, 1983.

Moulin, C., C. E. Lambert, F. Dulac, and U. Dayan, Control of atmospheric export of dust from North Africa by the North Atlantic Oscillation, *Nature*, *387*, 691-694, 1997.

Murayama, T., H. Okamoto, N. Kaneyasu, H. Kamataki, and K. Miura, Application of lidar depolarization measurement in the atmospheric boundary layer: Effects of dust and sea-salt particles, *J. Geophys. Res.*, *104*, 31,781-31,792, 1999.

Nakajima, T., and A. Higurashi, A use of two-channel radiances for an aerosol characterization from space, *Geophys. Res. Lett.*, *25*, 3815-3818, 1998.

Nakajima, T., and M. Tanaka, Matrix formulations for the transfer of solar radiation in a plane-parallel scattering atmosphere, *J. Quant. Spectrosc. Radiat. Transfer*, *35*, 13-21, 1986.

Nguyen, B. C., N. Mihalopoulos, J. P. Putaud, A. Gaudry, L. Gallet, W. C. Keene, and J. N. Galloway, Covariations in oceanic dimethyl sulfide, its oxidation products and rain acidity at Amsterdam Island in the southern Indian Ocean, *J. Atmos. Chem.*, *15*, 39-53, 1992.

Novakov, T., and J. E. Penner, Large contribution of organic aerosols to cloud-condensation-nuclei concentrations, *Nature*, *365*, 823-826, 1993.

Novakov, T., D. A. Hegg, and P. V. Hobbs, Airborne measurements of carbonaceous aerosols on the east coast of the United States, *J. Geophys. Res.*, *102*, 30,023-30,030, 1997.

Numaguti, A., Dynamics and energy balance of the Hadley circulation and the tropical precipitation zones: Significance of the distribution of evaporation, *J. Atmos. Sci.*, *50*, 1874-1887, 1993.

Numaguti, A., M. Takahashi, T. Nakajima, and A. Sumi, Development of an atmospheric general circulation model, in *Climate System Dynamics and Modeling*, edited by T. Matsuno, pp. 1-27, Center for Climate System Research, University of Tokyo, Tokyo, 1995.

Okamoto, H., A. Macke, M. Quante, and E. Raschke, Modeling of backscattering by non-spherical ice particles for the interpretation of cloud radar signals at 94 GHz: An error analysis, *Contrib. Atmos. Phys.*, *68*, 319-334, 1995.

Pandis, S. N., S. E. Paulson, J. H. Seinfeld, and R. C. Flagan, Aerosol formation in the photooxidation of isoprene and β-pinene, *Atmos. Environ., Ser. A*, *25*, 997-1008, 1991.

Parungo, F., C. Nagamoto, M. Y. Zhou, A. D. A. Hansen, and J. Harris, Aeolian transport of aerosol black carbon from China to the ocean, *Atmos. Environ.*, *28*, 3251-3260, 1994.

Penner, J. E., C. C. Chuang, and K. Grant, Climate forcing by carbonaceous and sulfate aerosols, *Clim. Dyn.*, *14*, 839-851, 1998.

Pham, M., J. F. Müller, G. P. Brasseur, C. Granier, and G. Mégie, A three-dimensional study of the tropospheric sulfur cycle, *J. Geophys. Res.*, *100*, 26,061-26,092, 1995.

Prospero, J. M., and T. N. Carlson, Vertical and areal distribution of Saharan dust over the western equatorial North Atlantic Ocean, *J. Geophys. Res.*, *77*, 5255-5265, 1972.

Prospero, J. M., D. L. Savoie, R. Arimoto, H. Olafsson, and H.

Hjarearson, Sources of aerosol nitrate and non-sea-salt sulfate in the Iceland region, *Sci. Total Environ.*, *160/161*, 181-191, 1995.

Pszenny, A. A., G. R. Harvey, C. J. Brown, R. F. Lang, W. C. Keene, J. N. Galloway, and J. T. Merrill, Measurements of dimethyl sulfide oxidation products in the summertime North Atlantic marine boundary layer, *Global Biochem. Cycles*, *4*, 367-379, 1990.

Quinn, P. K., T. S. Bates, J. E. Jhonson, D. S. Covert, and R. J. Charlson, Interactions between sulfur and reduced nitrogen cycles over the central Pacific Ocean, *J. Geophys. Res.*, *95*, 16,405-16,416, 1990.

Rao, C. R. N., L. L. Stowe, E. P. McClain, and J. Sapper, Development and application of aerosols remote sensing with AVHRR data from the NOAA satellites, in *Aerosol and Climate*, edited by P. V. Hobbs and M. P. McCormick, pp. 69-79, A. Deepak, Hampton, Virginia, 1988.

Saltzman, E. S., and D. J. Cooper, Shipboard measurements of atmospheric dimethylsulfide and hydrogen sulfide in the Caribbean and Gulf of Mexico, *J. Atmos. Chem.*, *7*, 191-209, 1988.

Savoie, D. L., J. M. Prospero, and E. S. Saitzman, Nitrate, non-seasalt sulfate and methane-sulfonate over the Pacific Ocean, in *Chemical Oceanography*, vol. 10, edited by J. P. Riley, R. Chester, and R. A. Duce, pp. 219-250, Academic, San Diego, Calif., 1989.

Savoie, D. L., J. M. Prospero, R. J. Larsen, F. Huang, M. Izaguirre, T. Huang, T. H. Snowdon, L. Custals, and C. G. Sanderson, Nitrogen and sulfur species in Antarctic aerosols at Mawson, Palmer Station, and Marsh (King George Island), *J. Atmos. Chem.*, *17*, 95-122, 1993.

Shaw, R. W., and R. J. Paur, Measurements of sulfur in gases and particles during sixteen months in the Ohio River Valley, *Atmos. Environ.*, *17*, 1431-1438, 1983.

Shettle, E. P., and R. W. Fenn, Models for the aerosols of the lower atmosphere and the effects of humidity variations on their optical properties, *Environ. Res. Pap.*, *676*, 94 pp., Air Force Geophys. Lab., Bedford, Mass., 1979.

Spivakovsky, C. M., R. Yevich, J. A. Logan, S. C. Wofsy, and M. B. McElroy, Tropospheric OH in a three-dimensional chemical tracer model: An assessment based on observations of CH_3CCl_3, *J. Geophys. Res.*, *95*, 18,441-18,471, 1990.

Staubes, R., and H. W. Georgii, Biogenic sulfur compounds in seawater and the atmosphere of the Antarctic region, *Tellus, Ser. B*, *45*, 127-137, 1993.

Tegen, I., and I. Fung, Contribution to the atmospheric mineral aerosol load from land surface modification, *J. Geophys. Res.*, *100*, 18,707-18,726, 1995.

Tegen, I., and R. Miller, A general circulation model study on the interannual variability of soil dust aerosol, *J. Geophys. Res.*, *103*, 25,975-25,995, 1998.

Tegen, I., P. Hollrig, M. Chin, I. Fung, D. Jacob, and J. Penner, Contribution of different aerosol species to the global aerosol extinction optical thickness: Estimates from model results, *J. Geophys. Res.*, *102*, 23,895-23,915, 1997.

Twomey, S., Pollution and the planetary albedo, *Atmos. Environ.*, *8*, 1251-1256, 1974.

Volz, F. E., Infrared optical constants of ammonium sulfate, Sahara dust, volcanic pumice and flyash, *Appl. Opt.*, *12*, 564-568, 1973.

Warneck, P., *Chemistry of the Natural Atmosphere*, 757 pp., Academic, San Diego, Calif., 1988.

Weast, R. C. (Ed.), *Handbook of Chemistry and Physics*, CRC Press, Boca Ratou, Fla., 1976.

A. Higurashi, National Institute for Environmental Studies, 16-2 Onogawa, Tsukuba, Ibaraki 305-0053, Japan. (hakiko@nies.go.jp)

Y. Maruyama, T. Nakajima, and T. Takemura, Center for Climate System Research, University of Tokyo, 4-6-1 Komaba, Meguro-ku, Tokyo 153-8904, Japan. (maruyama@ssd.se.fujitsu.co.jp; teruyuki@ccsr.u-tokyo.ac.jp; toshi@ccsr.u-tokyo.ac.jp)

A. Numaguti, Graduate School of Environmental Earth Science, Hokkaido University, 10-5, Kita-ku, Sapporo 060-0810, Japan. (numa@ees.hokudai.ac.jp)

H. Okamoto, Kashima Space Research Center, Communications Research Laboratory, 893-1 Hirai, Kashima, Ibaraki 314-0012, Japan. (hokamoto@crl.go.jp)

(Received November 30, 1999; revised April 13, 2000;
accepted April 19, 2000.)